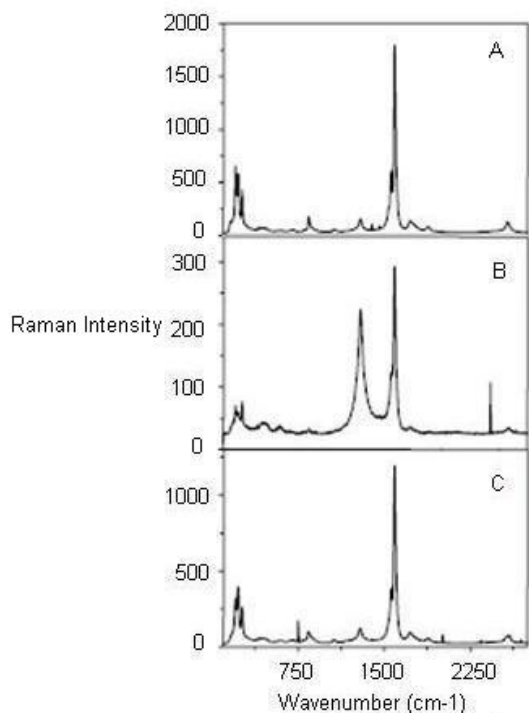


**Figure 3.63:** RBM frequencies  $\omega_{\text{RBM}} = A/d + B$  versus nanotube diameter for (i)  $A = 234 \text{ cm}^{-1} \text{ nm}$  and  $B = 10 \text{ cm}^{-1}$ , for SWNT bundles (dashed curve); (ii)  $A = 248 \text{ cm}^{-1} \text{ nm}$  and  $B = 0$ , for isolated SWNTs (solid curve). Adapted from A. Jorio, M. A. Pimenta, A. G. S. Filho, R. Saito, G. Dresselhaus, and M. S. Dresselhaus, *New J. Phys.*, 2003, **5**, 139.

Hence, a single Raman measurement gives an idea of the tubes that are in resonance with the laser line, but does not give a complete characterization of the diameter distribution of the sample. However, by taking Raman spectra using many laser lines, a good characterization of the diameter distributions in the sample can be obtained. Also, natural line widths observed for isolated SWNTs are  $\omega_{\text{RBM}} = 3 \text{ cm}^{-1}$ , but as the tube diameter is increased, broadening is observed which is denoted by  $\Gamma_{\text{RBM}}$ . It has been observed that for  $d > 2 \text{ nm}$ ,  $\Gamma_{\text{RBM}} > 20 \text{ cm}^{-1}$ . For SWNT bundles, the line width does not reflect  $\Gamma_{\text{RBM}}$ , it rather reflects an ensemble of tubes in resonance with the energy of laser.

#### 3.3.3.3.1.1 Variation of RBM intensities upon functionalization

Functionalization of SWNTs leads to variations of relative intensities of RBM compared to the starting material (unfunctionalized SWNTs). Owing to the diameter dependence of the RBM frequency and the resonant nature of the Raman scattering process, chemical reactions that are sensitive to the diameter as well as the electronic structure, i.e., metallic or semiconducting of the SWNTs can be sorted out. The difference in Raman spectra is usually inferred by thermal defunctionalization, where the functional groups are removed by annealing. The basis of using annealing for defunctionalizing SWNTs is based on the fact that annealing restores the Raman intensities, in contrast to other treatments where a complete disintegration of the SWNTs occurs. Figure 3.64 shows the Raman spectra of the pristine, functionalized and annealed SWNTs. It can be observed that the absolute intensities of the radial breathing modes is drastically reduced after functionalization. This decrease can be attributed to vHs, which themselves are a consequence of translational symmetry of the SWNTs. Since the translational symmetry of the SWNTs is broken as a result of irregular distribution of the  $\text{sp}^3$ -sites due to the functionalization, these vHs are broadened and strongly reduced in intensity. As a result, the resonant Raman cross section of all modes is strongly reduced as well.



**Figure 3.64:** Raman spectra of sidewall functionalized SWNTs of (A) pristine material, (B) functionalized SWNTs, and (C) after annealing at 750 °C in Ar. Adapted from R. Graupner, *J. Raman Spectrosc.*, 2007, **38**, 673.

For an ensemble of functionalized SWNTs, a decrease in high wavenumber RBM intensities has been observed which leads to an inference that destruction of small diameter SWNT takes place. Also, after prolonged treatment with nitric acid and subsequent annealing in oxygen or vacuum, diameter enlargement of SWNTs is observed from the disappearance of RBMs from small diameter SWNTs and the appearance of new RBMs characteristic of SWNTs with larger diameters. In addition, laser irradiation seems to damage preferentially small diameter SWNTs. In all cases, the decrease of RBM intensities is either attributed to the complete disintegration of SWNTs or reduction in resonance enhancement of selectively functionalized SWNTs. However, change in RBM intensities can also have other reasons. One reason is doping induced bleaching of electronic transitions in SWNTs. When a dopant is added, a previously occupied electronic state can be filled or emptied, as a result of which  $E_f$  in the SWNTs is shifted. If this shift is large enough and the conduction band vHs corresponding to the respective  $E_{ii}$  transition that is excited by the laser light gets occupied (n-type doping) or the valence band vHs is emptied (p-type doping), the resonant enhancement is lost as the electronic transitions are quenched.

Sample morphology has also seen to affect the RBMs. The same unfunctionalized sample in different aggregation states gives rise to different spectra. This is because the transition energy,  $E_{ii}$  depends on the aggregation state of the SWNTs.

### 3.3.3.3.2 Tangential modes (G-band)

The tangential modes are the most intensive high-energy modes of SWNTs and form the so-called G-band, which is typically observed at around  $1600\text{ cm}^{-1}$ . For this mode, the atomic displacements occur along the circumferential direction (Figure 3.65). Spectra in this frequency can be used for SWNT characterization, independent of the RBM observation. This multi-peak feature can, for example, also be used for diameter characterization, although the information provided is less accurate than the RBM feature, and it gives information about the metallic character of the SWNTs in resonance with laser line.

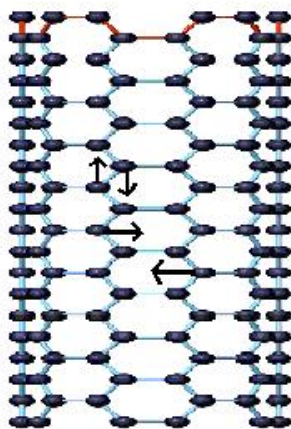


**Figure 3.65:** Schematic picture showing the atomic vibrations for the G-band. Adapted from A. Jorio, M. A. Pimenta, A. G. S. Filho, R. Saito, G. Dresselhaus, and M. S. Dresselhaus, *New J. Phys.*, 2003, **5**, 139.

The tangential modes are useful in distinguishing semiconducting from metallic SWNTs. The difference is evident in the G- feature (Figure 3.66 and Figure 3.67) which broadens and becomes asymmetric for metallic SWNTs in comparison with the Lorentzian lineshape for semiconducting tubes, and this broadening is related to the presence of free electrons in nanotubes with metallic character. This broadened G-feature is usually fit using a Breit-Wigner-Fano (BWF) line that accounts for the coupling of a discrete phonon with a continuum related to conduction electrons. This BWF line is observed in many graphite-like materials with metallic character, such as n-doped graphite intercalation compounds (GIC), n-doped fullerenes, as well as metallic SWNTs. The intensity of this G- mode depends on the size and number of metallic SWNTs in a bundle (Figure 3.68).

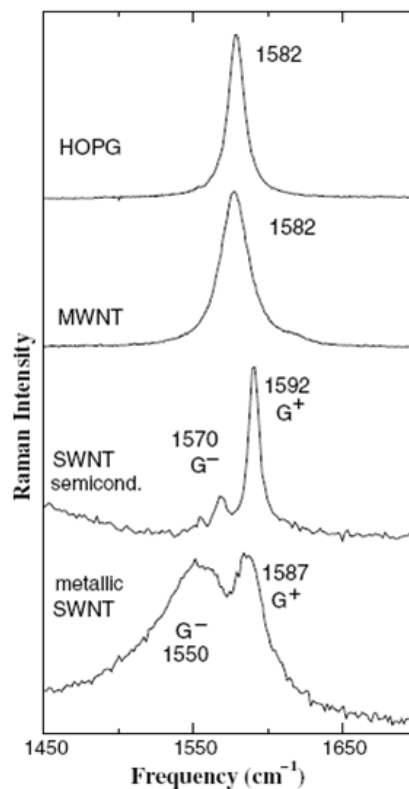


**Figure 3.66:** G-band for highly ordered pyrolytic graphite (HOPG), MWNT bundles, one isolated semiconducting SWNT and one isolated metallic SWNT. The multi-peak G-band feature is not clear for MWNTs due to the large tube size. A. Jorio, M. A. Pimenta, A. G. S. Filho, R. Saito, G. Dresselhaus, and M. S. Dresselhaus, *New J. Phys.*, 2003, **5**, 139. Copyright Institute of Physics (2005).



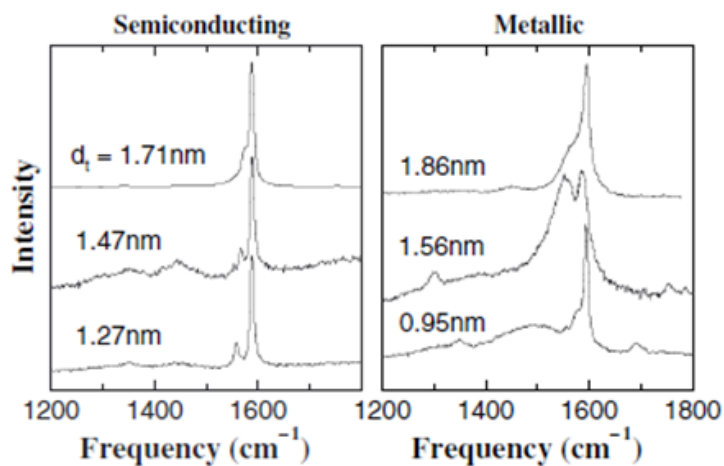


**Figure 3.67:** Raman signal from three isolated semiconducting and three isolated metallic SWNTs showing the G-and D-band profiles. SWNTs in good resonance (strong signal with low signal to noise ratio) show practically no D-band. A. Jorio, M. A. Pimenta, A. G. S. Filho, R. Saito, G. Dresselhaus, and M. S. Dresselhaus, *New J. Phys.*, 2003, **5**, 139. Copyright Institute of Physics (2005).

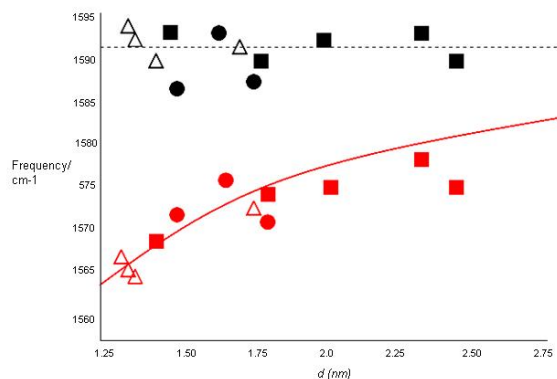


**Figure 3.68:** Dependence of G+ (black symbols) and G- (red symbols) frequencies as a function of diameter. Adapted from M. Paillet, T. Michel, J. C. Meyer, V. N. Popov, L. Henrad, S. Roth, and J. L. Sauvajol, *Phy. Rev. Lett.*, 2006, **96**, 257401.

### 3.3.3.3.2.1 Change of G-band line shape on functionalization

Chemical treatments are found to affect the line shape of the tangential line modes. Selective functionalization of SWNTs or a change in the ratio of metallic to semiconducting SWNTs due to selective etching is responsible for such a change. According to Figure 3.69, it can be seen that an increase or decrease of the BWF line shape is observed depending on the laser wavelength. At  $\lambda_{\text{exc}} = 633$  nm, the preferentially functionalized small diameter SWNTs are semiconducting, therefore the G-band shows a decrease in the BWF asymmetry. However, the situation is reversed at 514 nm, where small metallic tubes are probed. BWF resonance intensity of small bundles increases with bundle thickness, so care should be taken that the effect ascribed directly to functionalization of the SWNTs is not caused by the exfoliation of the previously bundles SWNT.

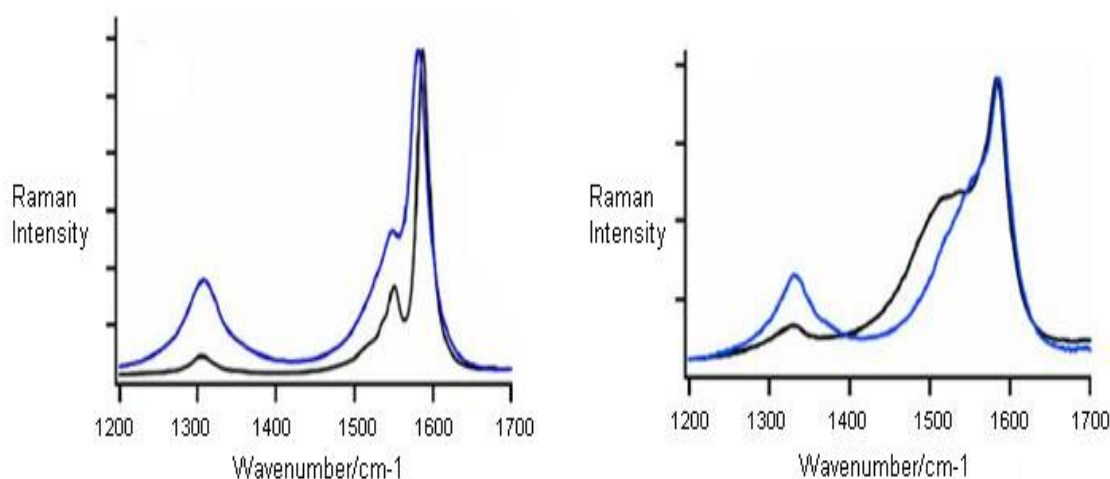


**Figure 3.69:** G-and D-band spectra of pristine (black) and ozonized (blue) SWNTs at 633 nm (left) and 514 nm (right) excitation. Adapted from R. Graupner, *J. Raman Spectrosc.*, 2007, **38**, 673.

### 3.3.3.3.3 Disorder-induced D-band

This is one of the most discussed modes for the characterization of functionalized SWNTs and is observed at  $1300\text{--}1400\text{ cm}^{-1}$ . Not only for functionalized SWNTs, D-band is also observed for unfunctionalized SWNTs. From a large number of Raman spectra from isolated SWNTs, about 50% exhibit observable D-band signals with weak intensity (Figure 3.67). A large D-peak compared with the G-peak usually means a bad resonance condition, which indicates the presence of amorphous carbon.

The appearance of D-peak can be interpreted due to the breakdown of the k-selection rule. It also depends on the laser energy and diameter of the SWNTs. This behavior is interpreted as a double resonance effect, where not only one of the direct, k-conserving electronic transitions, but also the emission of phonon is a resonant process. In contrast to single resonant Raman scattering, where only phonons around the center of the Brillouin zone ( $q = 0$ ) are excited, the phonons that provoke the D-band exhibit a non-negligible  $q$  vector. This explains the double resonance theory for D-band in Raman spectroscopy. In few cases, the overtone of the D-band known as the G'-band (or D\*-band) is observed at  $2600\text{--}2800\text{ cm}^{-1}$ , and it does not

require defect scattering as the two phonons with  $q$  and  $-q$  are excited. This mode is therefore observed independent of the defect concentration.

The presence of D-band cannot be correlated to the presence of various defects (such as hetero-atoms, vacancies, heptagon-pentagon pairs, kinks, or even the presence of impurities, etc). Following are the two main characteristics of the D-band found in carbon nanotubes:

1. Small linewidths:  $\Gamma_D$  values for SWNTs range from  $40\text{ cm}^{-1}$  down to  $7\text{ cm}^{-1}$ .
2. Lower frequencies: D-band frequency is usually lower than the frequency of  $\text{sp}^2$ -based carbons, and this downshift of frequency shows  $1/d$  dependence.

### 3.3.3.3.1 D-Band intensity as a measure of functionalization versus defect density

Since D-peak appears due to the presence defects, an increase in the intensity of the band is taken as a fingerprint for successful functionalization. But, whether D-band intensity is a measure of degree of functionalization or not is still sure. So, it is not correct to correlate D-peak intensity or D-peak area to the degree of functionalization. From Figure 3.70, it can be observed that for lower degree of functionalization, intensity of the D-band scales linearly with defect density. As the degree of functionalization is further increased, both D and G-band area decrease, which is explained by the loss of resonance enhancement due to functionalization. Also, normalization of the D-peak intensity to the G-band in order to correct for changes in resonance intensities also leads to a decrease for higher densities of functional groups.

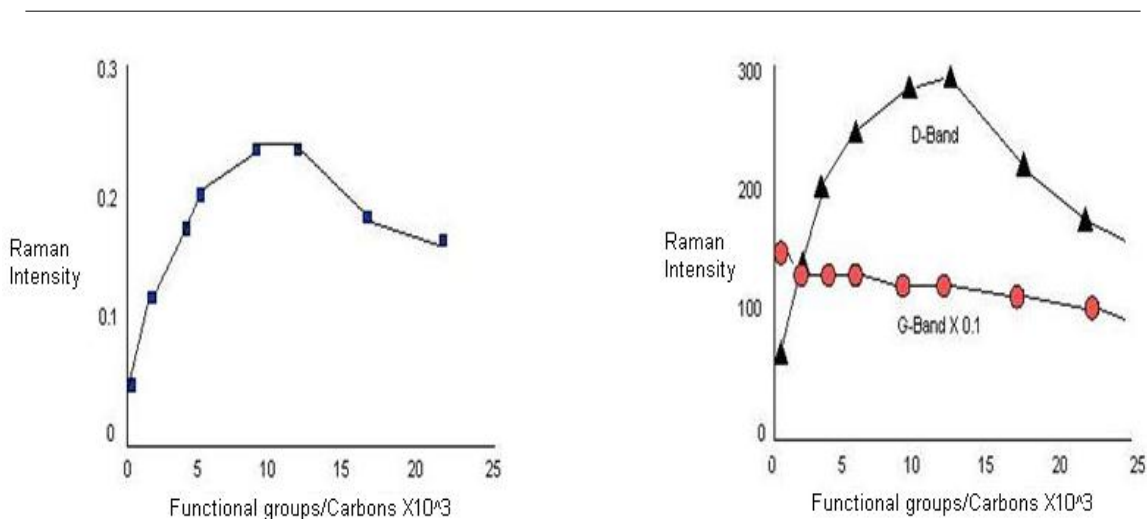


**Figure 3.70:** The left figure shows the intensity ratio  $I_D/I_G$  and the right figure shows D- and G-band intensity at  $\lambda_{\text{exc}} = 532\text{ nm}$  with respect to degree of functionalization using diazonium reagents. Adapted from R. Graupner, *J. Raman Spectrosc.*, 2007, **38**, 673.

### 3.3.3.3.4 Limitations of Raman spectroscopy

Though Raman spectroscopy has provides an exceedingly important tool for characterization of SWNTs, however, it suffers from few serious limitations. One of the main limitations of Raman spectroscopy is that it does not provide any information about the extent of functionalization in the SWNTs. The presence of

D-band indicates disorder, i.e. side wall distribution, however it cannot differentiate between the number of substituents and their distribution. Following are the two main limitations of Raman Spectroscopy:

#### 3.3.3.3.4.1 Quantification of substituents

This can be illustrated by the following examples. Purified HiPco tubes may be fluorinated at 150 °C to give F-SWNTs with a C:F ratio of approximately 2.4:1. The Raman spectra (using 780 nm excitation) for F-SWNTs shows in addition to the tangential mode at  $\sim 1587\text{ cm}^{-1}$  an intense broad D (disorder) mode at  $\sim 1295\text{ cm}^{-1}$  consistent with the side wall functionalization. Irrespective of the arrangements of the fluorine substituents, thermolysis of F-SWNTs results in the loss of fluorine and the re-formation of unfunctionalized SWNTs along with their cleavage into shorter length tubes. As can be seen from Figure 3.71, the intensity of the D-band decreases as the thermolysis temperature increases. This is consistent with the loss of F-substituents. The G-band shows a concomitant sharpening and increase in intensity.

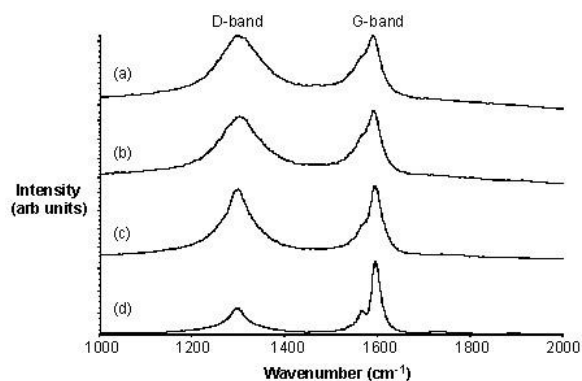


**Figure 3.71:** Raman spectra of F-SWNTs (a) as prepared at 150 °C and after heating to (b) 400, (c) 450 and (d) 550 °C.

As discussed above, the presence of a significant D mode has been the primary method for determining the presence of sidewall functionalization. It has been commonly accepted that the relative intensity of the D mode *versus* the tangential G mode is a quantitative measure of level of substitution. However, as discussed below, the G:D ratio is also dependent on the distribution of substituents. Using Raman spectroscopy in combination with XPS analysis of F-SWNTs that have been subjected to thermolysis at different temperatures, a measure of the accuracy of Raman as a quantitative tool for determining substituent concentration can be obtained. As can be seen from Figure 3.72, there is essentially no change in the G:D band ratio despite a doubling amount of functional groups. Thus, at low levels of functionalization the use of Raman spectroscopy to quantify the presence of fluorine substituents is a clearly suspect.

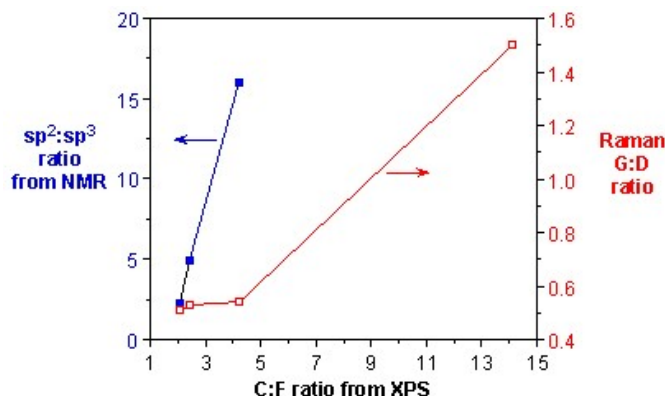


**Figure 3.72:** C(sp<sup>2</sup>):C-F(sp<sup>3</sup>) ratio (blue) and Raman G-band:D-band ratio (red) as a function of C:F ratio from XPS.

On the basis of above data it can be concluded that Raman spectroscopy does not provide an accurate quantification of small differences at low levels of functionalization, whereas when a comparison between samples with high levels of functionalization or large differences in degree of functionalization is required, Raman spectroscopy provides a good quantification.

#### 3.3.3.3.4.2 Number versus distribution

Fluorinated nanotubes may be readily functionalized by reaction with the appropriate amine in the presence of base according to the scheme shown in Figure 3.73.

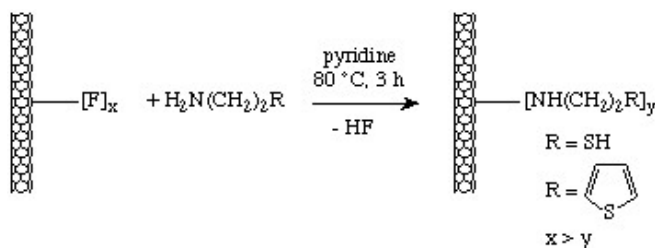


**Figure 3.73:** Synthesis of functionalized SWNTs.

When the Raman spectra of the functionalized SWNTs is taken (Figure 3.74), it is found out that the relative intensity of the disorder D-band at  $\sim 1290\text{ cm}^{-1}$  versus the tangential G-band ( $1500 - 1600\text{ cm}^{-1}$ ) is much higher for thiophene-SWNT than thiol-SWNT. If the relative intensity of the D mode is the measure of the level of substitution, it can be concluded that there are more number of thiophene groups present per C than thiol groups. However, from the TGA weight loss data the SWNT-C:substituent ratios are calculated to be 19:1 and 17.5:1. Thus, contrary to the Raman data the TGA suggest that the number of substituents per C (in the SWNT) is actually similar for both substituents.

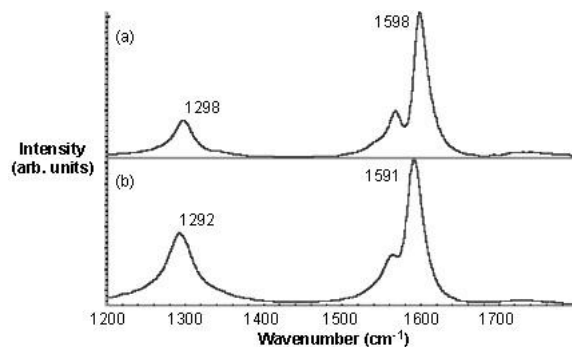


**Figure 3.74:** Raman spectrum of (a) thiol-SWNT and (b) thiophene-SWNT using 780 nm excitation showing the relative intensity of D-band at  $\sim 1300\text{ cm}^{-1}$  versus the G-band at  $\sim 1590\text{ cm}^{-1}$ .

This result would suggest that Raman spectroscopy is potentially unsuccessful in correctly providing the information about the number of substituents on the SWNTs. Subsequent imaging of the functionalized SWNTs by STM showed that the distribution of the functional groups was the difference between the thiol and thiophene functionalized SWNTs Figure 3.75. Thus, relative ratio of the D- and G-bands is a measure of concentration and distribution of functional groups on SWNTs.

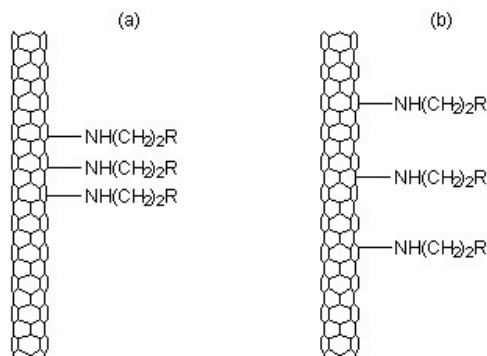


**Figure 3.75:** Schematic representation of the functional group distribution for (a) thiol-SWNT and (b) thiophene-SWNT.

### 3.3.3.4 Multi-walled carbon nanotubes (MWNTs)

Most of the characteristic differences that distinguish the Raman spectra in SWNTs from the spectra of graphite are not so evident for MWNTs. It is because the outer diameter for MWNTs is very large and the ensemble of CNTs in them varies from small to very large. For example, the RBM Raman feature associated with a small diameter inner tube (less than 2 nm) can sometimes be observed when a good resonance condition is established, but since the RBM signal from large diameter tubes is usually too weak

to be observable and the ensemble average of inner tube diameter broadens the signal, a good signal is not observed. However, when hydrogen gas in the arc discharge method is used, a thin innermost nanotube within a MWNT of diameter 1 nm can be obtained which gives strong RBM peaks in the Raman spectra.

Thereas the G+ - G- splitting is large for small diameter SWNT, the corresponding splitting of the G-band in MWNTs is both small in intensity and smeared out due to the effect of the diameter distribution. Therefore the G-band feature predominantly exists a weakly asymmetric characteristic lineshape, and a peak appearing close to the graphite frequency of  $1582\text{ cm}^{-1}$ . however for isolated MWNTs prepared in the presence of hydrogen gas using the arc discharge method, it is possible to observe multiple G-band splitting effects even more clearly than for the SWNTs, and this is because environmental effects become relatively small for the innermost nanotube in a MWNT relative to the interactions occurring between SWNTs and different environments. The Raman spectroscopy of MWNTs has not been well investigated up to now. The new directions in this field are yet to be explored.

### 3.3.3.5 Bibliography

- R. Graupner, *J. Ramn Spectrosc.*, 2007, **38**, 673.
- S. Costa, B. Palen, M. Kruszynska, A. Bachmatiuk, and R.J. Kalenczuk, *Mat. Sci. Poland*, 2008, **26**, 433.
- M. Paillet, T. Michel, J. C. Meyer, V. N. Popov, L. Henrad, S. Roth, and J. L. Sauvajol, *Phy. Rev. Lett.*, 2006, **96**, 257401.
- L. Zhang, J. Zhang, N. Schmandt, J. Cratty, V. N. Khabashesku, K. F. Kelly, and A. R. Barron, *Chem. Commun.*, 2005, 5429.
- L. B. Alemany, L. Zhang, L. Zeng, C. L. Edwards, and A. R. Barron, *Chem. Mater.*, 2006, **19**, 735.
- M. S. Dresselhaus, G. Dresselhaus, R. Saito, and A. Jorio, *J. Phys. Rep.*, 2005, **2**, 47.
- A. Jorio, M. A. Pimenta, A. G. S. Filho, R. Saito, G. Dresselhaus, and M. S. Dresselhaus, *New J. Phys.*, 2003, **5**, 139.

## 3.4 UV-Visible Spectroscopy

### 3.4.1 Basics of UV-Visible Spectroscopy<sup>11</sup>

#### 3.4.1.1 Introduction

Ultraviolet-visible (UV-vis) spectroscopy is used to obtain the absorbance spectra of a compound in solution or as a solid. What is actually being observed spectroscopically is the absorbance of light energy or electromagnetic radiation, which excites electrons from the ground state to the first singlet excited state of the compound or material. The UV-vis region of energy for the electromagnetic spectrum covers 1.5 - 6.2 eV which relates to a wavelength range of 800 - 200 nm. The Beer-Lambert Law, (3.7), is the principle behind absorbance spectroscopy. For a single wavelength,  $A$  is absorbance (unitless, usually seen as arb. units or arbitrary units),  $\epsilon$  is the molar absorptivity of the compound or molecule in solution ( $\text{M}^{-1}\text{cm}^{-1}$ ),  $b$  is the path length of the cuvette or sample holder (usually 1 cm), and  $c$  is the concentration of the solution (M).

$$A = \epsilon bc \tag{3.7}$$

There are three types of absorbance instruments used to collect UV-vis spectra:

- 1) Single beam spectrometer.
- 2) Double beam spectrometer.
- 3) Simultaneous spectrometer.

<sup>11</sup>This content is available online at <<http://cnx.org/content/m34525/1.1/>>.

All of these instruments have a light source (usually a deuterium or tungsten lamp), a sample holder and a detector, but some have a filter for selecting one wavelength at a time. The single beam instrument (Figure 3.76) has a filter or a monochromator between the source and the sample to analyze one wavelength at a time. The double beam instrument (Figure 3.77) has a single source and a monochromator and then there is a splitter and a series of mirrors to get the beam to a reference sample and the sample to be analyzed, this allows for more accurate readings. In contrast, the simultaneous instrument (Figure 3.78) does not have a monochromator between the sample and the source; instead, it has a diode array detector that allows the instrument to simultaneously detect the absorbance at all wavelengths. The simultaneous instrument is usually much faster and more efficient, but all of these types of spectrometers work well.

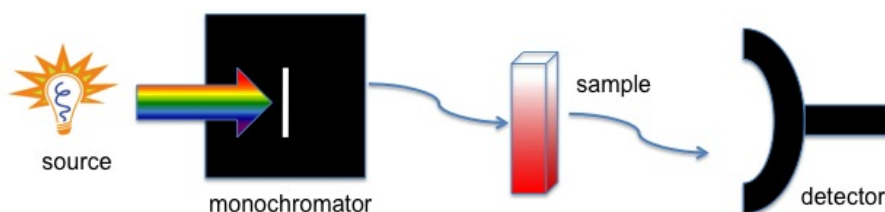


**Figure 3.76:** Illustration of a single beam UV-vis instrument.

---

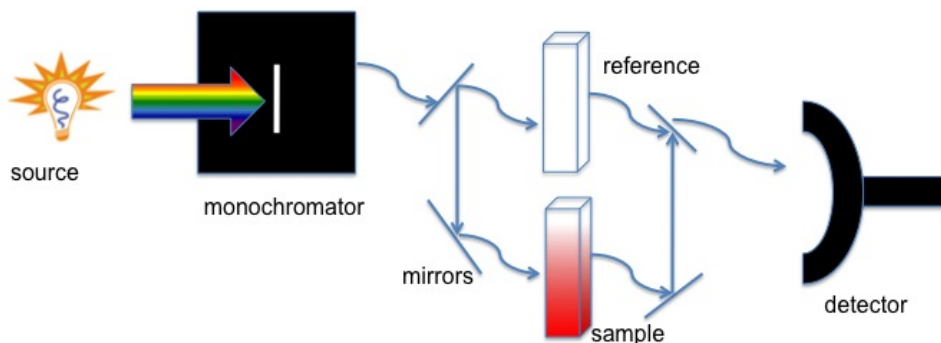


**Figure 3.77:** Illustration of a double beam UV-vis instrument.

---



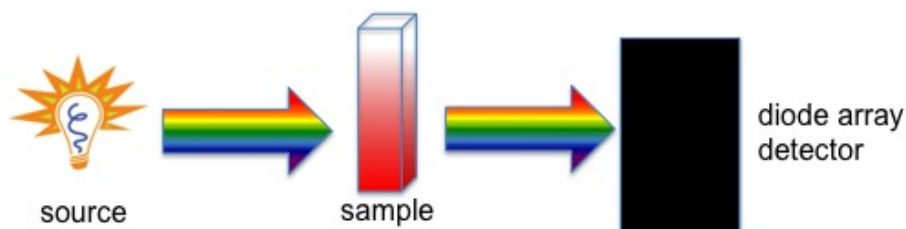


**Figure 3.78:** Illustration of a simultaneous UV-vis instrument.

---

#### 3.4.1.2 What information can be obtained from UV-vis spectra?

UV-vis spectroscopic data can give qualitative and quantitative information of a given compound or molecule. Irrespective of whether quantitative or qualitative information is required it is important to use a reference cell to zero the instrument for the solvent the compound is in. For quantitative information on the compound, calibrating the instrument using known concentrations of the compound in question in a solution with the same solvent as the unknown sample would be required. If the information needed is just proof that a compound is in the sample being analyzed, a calibration curve will not be necessary; however, if a degradation study or reaction is being performed, and concentration of the compound in solution is required, thus a calibration curve is needed.

To make a calibration curve, at least three concentrations of the compound will be needed, but five concentrations would be most ideal for a more accurate curve. The concentrations should start at just above the estimated concentration of the unknown sample and should go down to about an order of magnitude lower than the highest concentration. The calibration solutions should be spaced relatively equally apart, and they should be made as accurately as possible using digital pipettes and volumetric flasks instead of graduated cylinders and beakers. An example of absorbance spectra of calibration solutions of Rose Bengal (4,5,6,7-tetrachloro-2',4',5',7'-tetraiodofluorescein, Figure 3.79) can be seen in Figure 3.80. To make a calibration curve, the value for the absorbances of each of the spectral curves at the highest absorbing wavelength, is plotted in a graph similar to that in Figure 3.81 of absorbance versus concentration. The correlation coefficient of an acceptable calibration is 0.9 or better. If the correlation coefficient is lower than that, try making the solutions again as the problem may be human error. However, if after making the solutions a few times the calibration is still poor, something may be wrong with the instrument; for example, the lamps may be good.

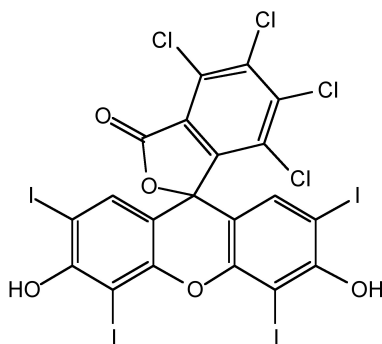


**Figure 3.79:** The molecular structure of Rose Bengal (4,5,6,7-tetrachloro-2',4',5',7'-tetraiodofluorescein).

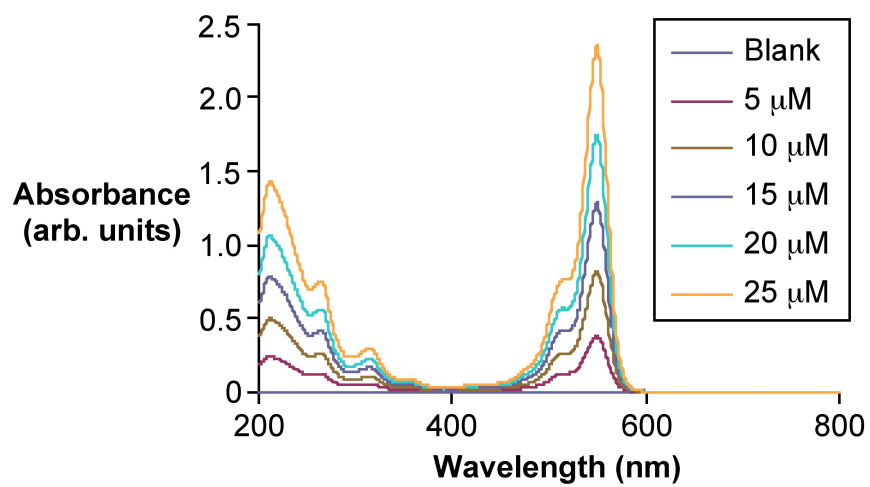


**Figure 3.80:** UV-vis spectra of different concentrations of Rose Bengal.

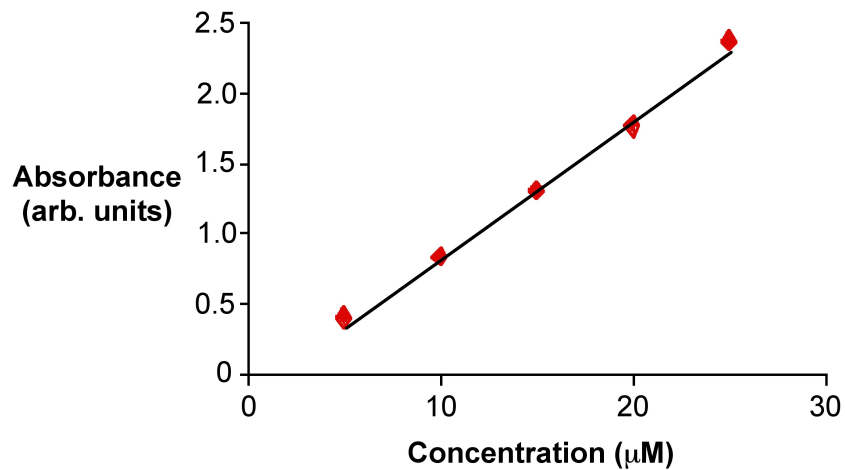


**Figure 3.81:** Calibration curve of Rose Bengal. Equation of line:  $y = 0.0977x - 0.1492$  ( $R^2 = 0.996$ )

---

### 3.4.1.3 Limitations of UV-visible spectroscopy

#### 3.4.1.3.1 Sample

UV-vis spectroscopy works well on liquids and solutions, but if the sample is more of a suspension of solid particles in liquid, the sample will scatter the light more than absorb the light and the data will be very skewed. Most UV-vis instruments can analyze solid samples or suspensions with a diffraction apparatus (Figure 3.82), but this is not common. UV-vis instruments generally analyze liquids and solutions most efficiently.

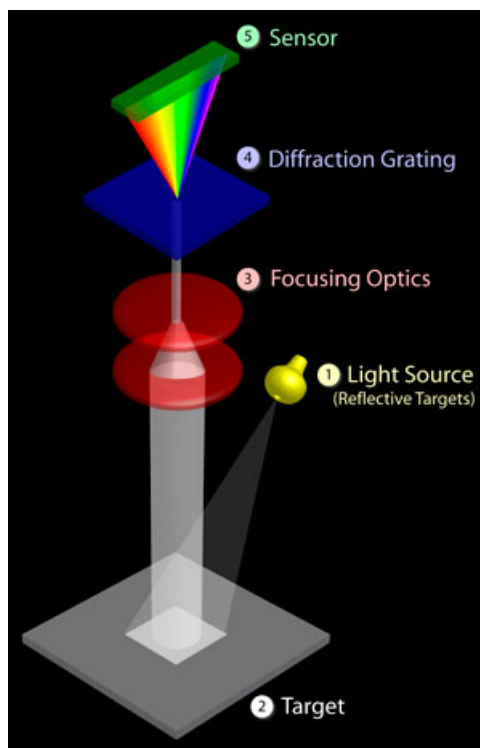


**Figure 3.82:** Schematic representation of the apparatus for collecting UV-vis spectra from solid materials.

#### 3.4.1.3.2 Calibration and reference

A blank reference will be needed at the very beginning of the analysis of the solvent to be used (water, hexanes, etc), and if concentration analysis needs to be performed, calibration solutions need to be made accurately (e.g., Figure 3.81). If the solutions are not made accurately enough, the actual concentration of the sample in question will not be accurately determined.

#### 3.4.1.3.3 Choice of solvent or container

Every solvent has a UV-vis absorbance cutoff wavelength. The solvent cutoff is the wavelength below which the solvent itself absorbs all of the light. So when choosing a solvent be aware of its absorbance cutoff and where the compound under investigation is thought to absorb. If they are close, chose a different solvent. Table 3.11 provides an example of solvent cutoffs.

Solvent	UV absorbance cutoff (nm)
Acetone	329
Benzene	278
Dimethylformamide (DMF)	267
Ethanol	205
Toluene	285
Water	180

**Table 3.11:** UV absorbance cutoffs of various common solvents.

The material the cuvette (the sample holder) is made from will also have a UV-vis absorbance cutoff. Glass will absorb all of the light higher in energy starting at about 300 nm, so if the sample absorbs in the UV, a quartz cuvette will be more practical as the absorbance cutoff is around 160 nm for quartz (Table 3.12).

Material	Wavelength range (nm)
Glass	380 - 780
Plastic	380 - 780
Fused quartz	below 380

**Table 3.12:** Three different types of cuvettes commonly used, with different usable wavelengths.

#### 3.4.1.3.4 Concentration of solution

To obtain reliable data, the peak of absorbance of a given compound needs to be at least three times higher in intensity than the background noise of the instrument. Obviously using higher concentrations of the compound in solution can combat this. Also, if the sample is very small and diluting it would not give an acceptable signal, there are cuvettes that hold smaller sample sizes than the 2.5 mL of a standard cuvettes. Some cuvettes are made to hold only 100  $\mu\text{L}$ , which would allow for a small sample to be analyzed without having to dilute it to a larger volume, lowering the signal to noise ratio.

#### 3.4.1.4 Bibliography

- D. A. Skoog, F. J. Holler, S. R. Crouch, *Principles of Instrumental Analysis*, 6<sup>th</sup> Ed., Thomson Brooks/Cole (2007).
- J. P. Sibilio, *Materials Characterization and Chemical Analysis*, 2<sup>nd</sup> Ed., Wiley-VCH, New York (1996).
- D. C. Harris, *Quantitative Chemical Analysis*, 7<sup>th</sup> Ed., Freeman, New York(2007).

## 3.5 Photoluminescence and Fluorescence Spectroscopy

### 3.5.1 Photoluminescence Spectroscopy and its Applications<sup>12</sup>

#### 3.5.1.1 Introduction

##### 3.5.1.1.1 What is photoluminescence

Photoluminescence spectroscopy is a contactless, nondestructive method of probing the electronic structure of materials. Light is directed onto a sample, where it is absorbed and imparts excess energy into the material in a process called *photo-excitation*. One way this excess energy can be dissipated by the sample is through the emission of light, or *luminescence*. In the case of photo-excitation, this luminescence is called *photoluminescence*.

Photo-excitation causes electrons within a material to move into permissible excited states. When these electrons return to their equilibrium states, the excess energy is released and may include the emission of light (a radiative process) or may not (a nonradiative process). The energy of the emitted light (photoluminescence) relates to the difference in energy levels between the two electron states involved in the transition between the excited state and the equilibrium state. The quantity of the emitted light is related to the relative contribution of the radiative process.

##### 3.5.1.1.2 The importance of photoluminescence

In most photoluminescent systems chromophore aggregation generally quenches light emission via aggregation-caused quenching (ACQ). This means that it is necessary to use and study fluorophores in dilute solutions or as isolated molecules. This in turn results in poor sensitivity of devices employing fluorescence, e.g., biosensors and bioassays. However, there have recently been examples reported in which luminogen aggregation played a constructive, instead of destructive role in the light-emitting process. This aggregated-induced emission (AIE) is of great potential significance in particular with regard to solid state devices. Photoluminescence spectroscopy provides a good method for the study of luminescent properties of a fluorophore.

##### 3.5.1.1.3 Forms of photoluminescence

###### 3.5.1.1.3.1 Resonant radiation

In resonant radiation, a photon of a particular wavelength is absorbed and an equivalent photon is immediately emitted, through which no significant internal energy transitions of the chemical substrate between absorption and emission are involved and the process is usually of an order of 10 nanoseconds.

###### 3.5.1.1.3.2 Fluorescence

When the chemical substrate undergoes internal energy transitions before relaxing to its ground state by emitting photons, some of the absorbed energy is dissipated so that the emitted light photons are of lower energy than those absorbed. One of such most familiar phenomenon is fluorescence, which has a short lifetime ( $10^{-8}$  to  $10^{-4}$  s).

###### 3.5.1.1.3.3 Phosphorescence

Phosphorescence is a radiational transition, in which the absorbed energy undergoes intersystem crossing into a state with a different spin multiplicity. The lifetime of phosphorescence is usually from  $10^{-4}$  -  $10^{-2}$  s, much longer than that of Fluorescence. Therefore, phosphorescence is even rarer than fluorescence, since a molecule in the triplet state has a good chance of undergoing intersystem crossing to ground state before phosphorescence can occur.

<sup>12</sup>This content is available online at <<http://cnx.org/content/m38357/1.2/>>.

#### 3.5.1.1.4 Relation between absorption and emission spectra

Fluorescence and phosphorescence come at lower energy than absorption (the excitation energy). As shown in Figure 3.83, in absorption, wavelength  $\lambda_0$  corresponds to a transition from the ground vibrational level of  $S_0$  to the lowest vibrational level of  $S_1$ . After absorption, the vibrationally excited  $S_1$  molecule relaxes back to the lowest vibrational level of  $S_1$  prior to emitting any radiation. The highest energy transition comes at wavelength  $\lambda_0$ , with a series of peaks following at longer wavelength. The absorption and emission spectra will have an approximate mirror image relation if the spacings between vibrational levels are roughly equal and if the transition probabilities are similar. The  $\lambda_0$  transitions in Figure 3.84 do not exactly overlap. As shown in Figure 3.83, a molecule absorbing radiation is initially in its electronic ground state,  $S_0$ . This molecule possesses a certain geometry and solvation. As the electronic transition is faster than the vibrational motion of atoms or the translational motion of solvent molecules, when radiation is first absorbed, the excited  $S_1$  molecule still possesses its  $S_0$  geometry and solvation. Shortly after excitation, the geometry and solvation change to their most favorable values for  $S_1$  state. This rearrangement lowers the energy of excited molecule. When an  $S_1$  molecule fluoresces, it returns to the  $S_0$  state with  $S_1$  geometry and solvation. This unstable configuration must have a higher energy than that of an  $S_0$  molecule with  $S_0$  geometry and solvation. The net effect in Figure 3.83 is that the  $\lambda_0$  emission energy is less than the  $\lambda_0$  excitation energy.

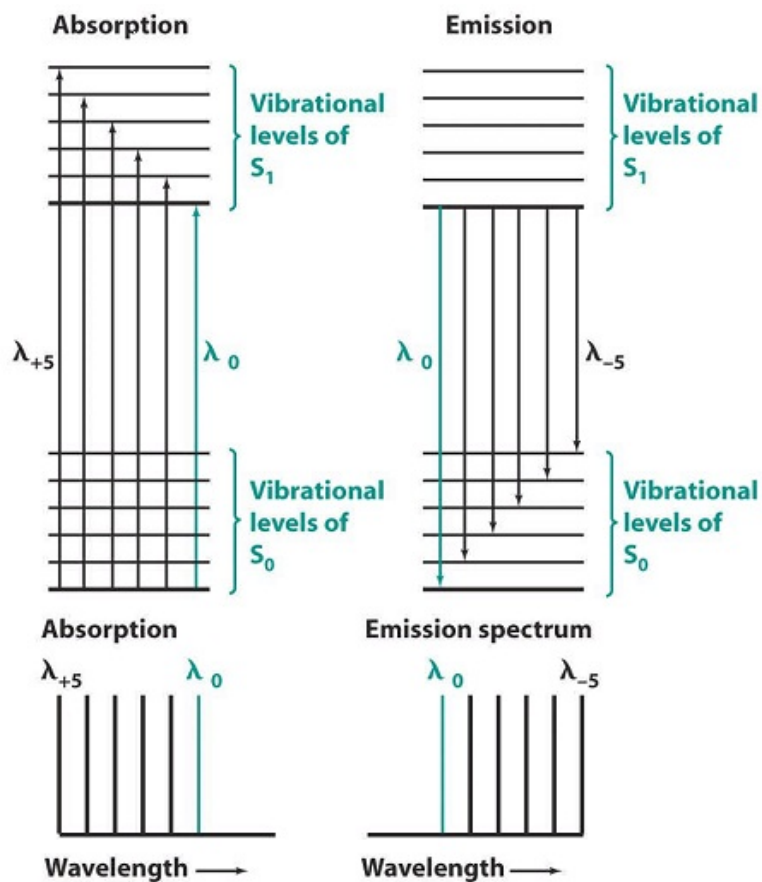


**Figure 3.83:** Energy-level diagram showing why structure is seen in the absorption and emission spectra and why the spectra are roughly mirror images of each other. Adapted from D. C. Harris, *Quantitative Chemical Analysis*, 7<sup>th</sup> Ed, W. H. Freeman and Company, New York (2006).



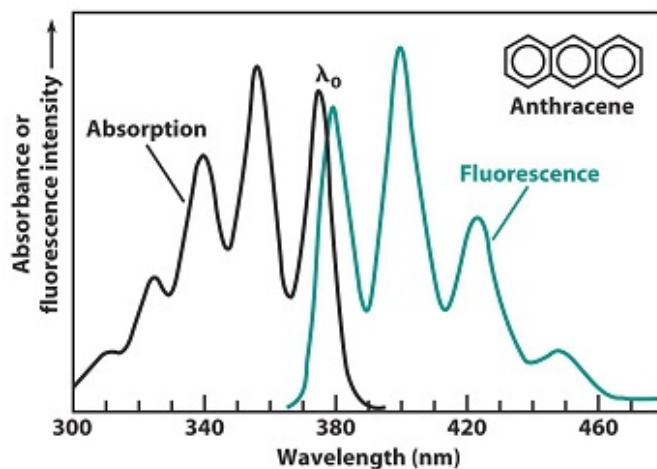


**Figure 3.84:** Excitation and emission spectra of anthracene that have the same mirror image relation at the absorption and emission spectra. Adapted from C. M. Byron and T. C. Werner, *J. Chem. Ed.*, 1991, **68**, 433.

### 3.5.1.2 Instrumentation

A schematic of an emission experiment is given in Figure 3.85. An excitation wavelength is selected by one monochromator, and luminescence is observed through a second monochromator, usually positioned at  $90^\circ$  to the incident light to minimize the intensity of scattered light reaching the detector. If the excitation wavelength is fixed and the emitted radiation is scanned, an emission spectrum is produced.

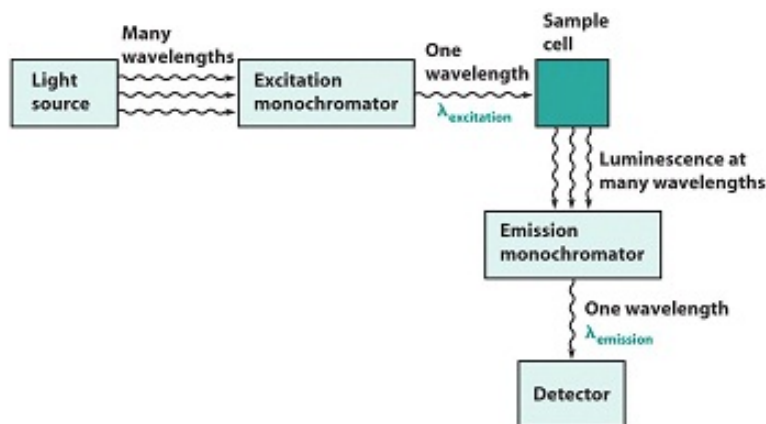


**Figure 3.85:** Essentials of a luminescence experiment. The sample is irradiated at one wavelength and emission is observed over a range of wavelengths. The excitation monochromator selects the excitation wavelength and the emission monochromator selects one wavelength at a time to observe. Adapted from D. C. Harris, *Quantitative Chemical Analysis*, 7<sup>th</sup> Edition, W. H. Freeman and Company, New York, (2006).

### 3.5.1.3 Relationship to UV-visible spectroscopy

Ultraviolet-visible (UV-vis) spectroscopy or ultraviolet-visible spectrophotometry refers to absorption spectroscopy or reflectance spectroscopy in the ultraviolet-visible spectral region. The absorption or reflectance in the visible range directly affects the perceived color of the chemicals involved. In the UV-vis spectrum, an absorbance versus wavelength graph results and it measures transitions from the ground state to excited state, while photoluminescence deals with transitions from the excited state to the ground state.

An excitation spectrum is a graph of emission intensity versus excitation wavelength. An excitation spectrum looks very much like an absorption spectrum. The greater the absorbance is at the excitation wavelength, the more molecules are promoted to the excited state and the more emission will be observed.

By running an UV-vis absorption spectrum, the wavelength at which the molecule absorbs energy most and is excited to a large extent can be obtained. Using such value as the excitation wavelength can thus provide a more intense emission at a red-shifted wavelength, which is usually within twice of the excitation wavelength.

### 3.5.1.4 Applications

#### 3.5.1.4.1 Detection of ACQ or AIE properties

Aggregation-caused quenching (ACQ) of light emission is a general phenomenon for many aromatic compounds that fluorescence is weakened with an increase in its solution concentration and even condensed phase. Such effect, however, comes into play in the solid state, which has prevented many lead luminogens identified by the laboratory solution-screening process from finding real-world applications in an engineering robust form.

Aggregation-induced emission (AIE), on the other hand, is a novel phenomenon that aggregation plays a constructive, instead of destructive role in the light-emitting process, which is exactly opposite to the ACQ effect.

#### 3.5.1.4.1.1 A case study

From the photoluminescence spectra of hexaphenylsilole (HPS, Figure 3.86) shown in Figure 3.87, it can be seen that as the water (bad solvent) fraction increases, the emission intensity of HPS increases. For BODIPY derivative (Figure 3.88) in Figure 3.89, it shows that the PL intensity peaks at 0 water content resulted from intramolecular rotation or twisting, known as *twisted intramolecular charge transfer* (TICT).

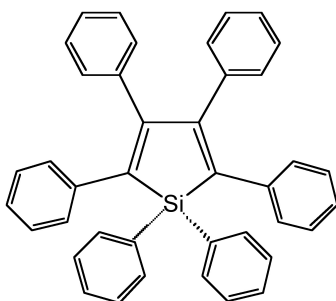


**Figure 3.86:** The structure of hexaphenylsilole (HPS).

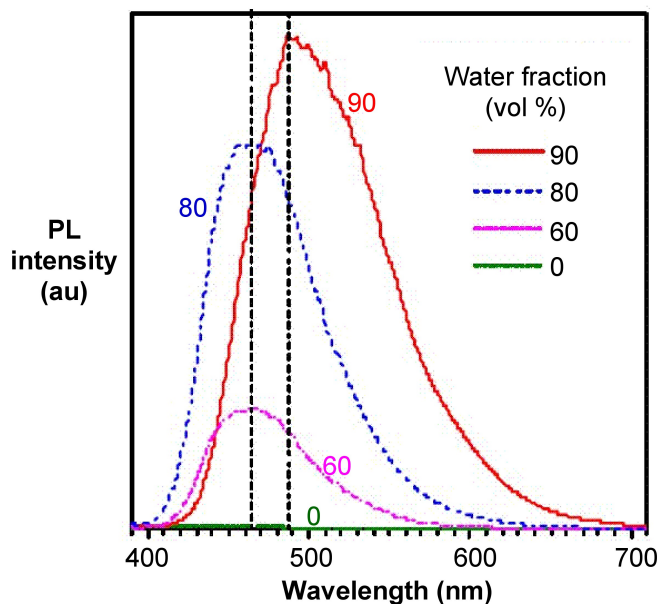


**Figure 3.87:** PL spectra of HPS solutions in acetonitrile/water mixtures. Adapted from Y. Hong, J. W. Y. Lam, and B. Z. Tang, *Chem. Commun.*, 2009, 4332. Copyright: The Royal Society of Chemistry (2009).

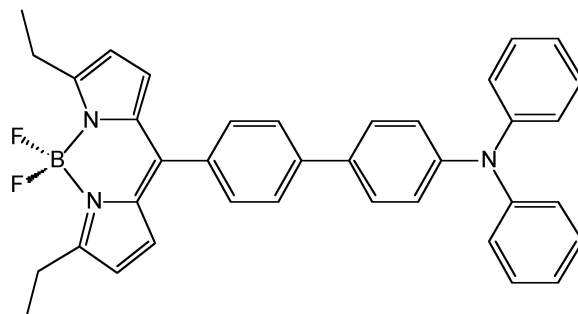


**Figure 3.88:** The structure of a triphenylamine–boradiazaindacene (BODIPY) derivative.

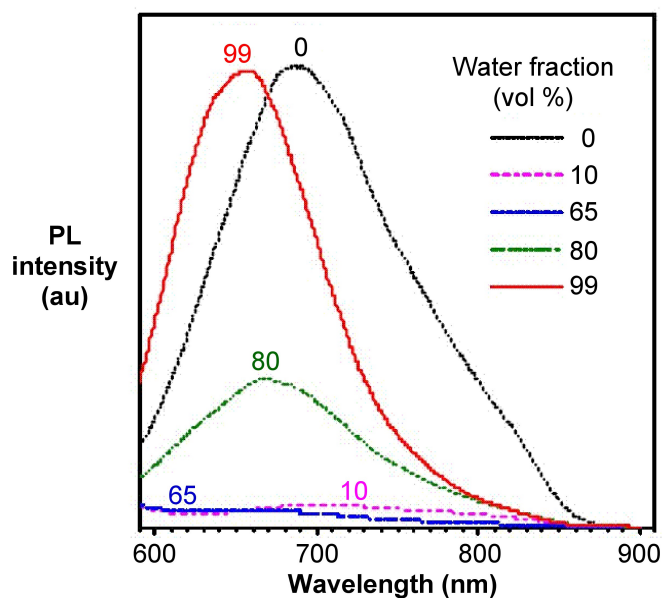


**Figure 3.89:** PL spectra of BODIPY derivative in THF/water mixtures. Adapted from Y. Hong, J. W. Y. Lam, and B. Z. Tang, *Chem. Commun.*, 2009, 4332. Copyright: The Royal Society of Chemistry (2009).

The emission color of an AIE luminogen is scarcely affected by solvent polarity, whereas that of a TICT luminogen typically bathochromically shifts with increasing solvent polarity. In Figure 3.90, however, it shows different patterns of emission under different excitation wavelengths. At the excitation wavelength of 372 nm, which is corresponding to the BODIPY group, the emission intensity increases as water fraction increases. However, it decreases at the excitation wavelength of 530 nm, which is corresponding to the TPE group. The presence of two emissions in this compound is due to the presence of two independent groups in

the compound with AIE and ACQ properties, respectively.

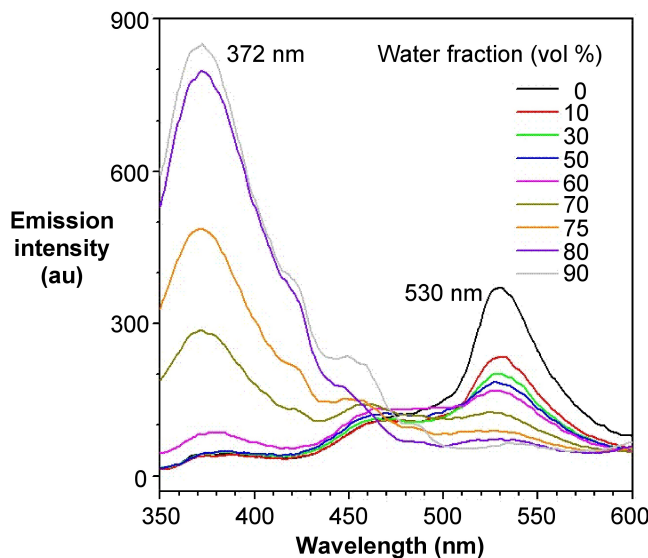


**Figure 3.90:** PL spectra of compound containing AIE and ACQ groups in THF/water mixtures at the excitation wavelength of 329 nm. Adapted from Y. Hong, J. W. Y. Lam, and B. Z. Tang, *Chem. Commun.*, 2009, 4332. Copyright: The Royal Society of Chemistry (2009).

#### 3.5.1.4.1.2 Detection of luminescence with respect to molarity

Figure 3.91 shows the photoluminescence spectroscopy of a BODIPY-TPE derivative of different concentrations. At the excitation wavelength of 329 nm, as the molarity increases, the emission intensity decreases. Such compounds whose PL emission intensity enhances at low concentration can be a good chemo-sensor for the detection of the presence of compounds with low quantity.

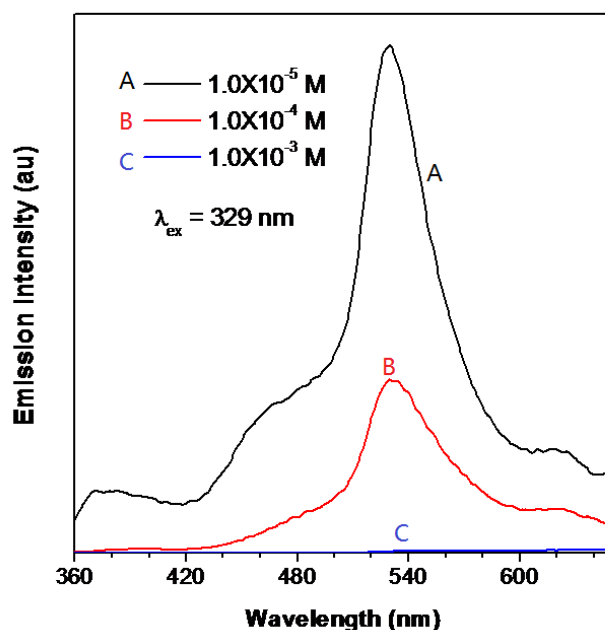


**Figure 3.91:** PL spectra of a BODIPY derivative solution in different concentrations in THF at excitation wavelength of 329 nm.

#### 3.5.1.4.2 Other applications

Apart from the detection of light emission patterns, photoluminescence spectroscopy is of great significance in other fields of analysis, especially semiconductors.

##### 3.5.1.4.2.1 Band gap determination

Band gap is the energy difference between states in the conduction and valence bands, of the radiative transition in semiconductors. The spectral distribution of PL from a semiconductor can be analyzed to nondestructively determine the electronic band gap. This provides a means to quantify the elemental composition of compound semiconductor and is a vitally important material parameter influencing solar cell device efficiency.

##### 3.5.1.4.2.2 Impurity levels and defect detection

Radiative transitions in semiconductors involve localized defect levels. The photoluminescence energy associated with these levels can be used to identify specific defects, and the amount of photoluminescence can be used to determine their concentration. The PL spectrum at low sample temperatures often reveals spectral peaks associated with impurities contained within the host material. Fourier transform photoluminescence microspectroscopy, which is of high sensitivity, provides the potential to identify extremely low concentrations of intentional and unintentional impurities that can strongly affect material quality and device performance.

#### 3.5.1.4.2.3 Recombination mechanisms

The return to equilibrium, known as “recombination”, can involve both radiative and nonradiative processes. The quantity of PL emitted from a material is directly related to the relative amount of radiative and nonradiative recombination rates. Nonradiative rates are typically associated with impurities and the amount of photoluminescence and its dependence on the level of photo-excitation and temperature are directly related to the dominant recombination process. Thus, analysis of photoluminescence can qualitatively monitor changes in material quality as a function of growth and processing conditions and help understand the underlying physics of the recombination mechanism.

#### 3.5.1.4.2.4 Surface structure and excited states

The widely used conventional methods such as XRD, IR and Raman spectroscopy, are very often not sensitive enough for supported oxide catalysts with low metal oxide concentrations. Photoluminescence, however, is very sensitive to surface effects or adsorbed species of semiconductor particles and thus can be used as a probe of electron-hole surface processes.

#### 3.5.1.5 Limitations of photoluminescence spectroscopy

Very low concentrations of optical centers can be detected using photoluminescence, but it is not generally a quantitative technique. The main scientific limitation of photoluminescence is that many optical centers may have multiple excited states, which are not populated at low temperature.

The disappearance of luminescence signal is another limitation of photoluminescence spectroscopy. For example, in the characterization of photoluminescence centers of silicon no sharp-line photoluminescence from 969 meV centers was observed when they had captured self-interstitials.

#### 3.5.1.6 Bibliography

- Y. Hong, J. W. Y. Lam, and B. Z. Tang, *Chem. Commun.*, 2009, 4332.
- M. Anpo, M. Kondo, S. Coluccia, C. Louis, and M. Che, *J. Am. Chem. Soc.*, 1989, **111**, 8791.
- N. S. Sariciftci, *Primary Photoexcitations In Conjugated Polymers Molecular Exciton Versus Semiconductor Band Model*, World Scientific Publishing Company, Singapore (1997).
- D. C. Harris, *Quantitative Chemical Analysis*, 7<sup>th</sup> Ed, W. H. Freeman and Company, New York (2006).
- G. Davies, *Phys. Rep.*, 1989, **176**, 83.

### 3.5.2 Fluorescence Characterization and its Application in DNA Detection<sup>13</sup>

#### 3.5.2.1 Introduction to fluorescence

Luminescence is a process involving the emission of light from any substance, and occurs from electronically excited states of that substance. Normally, luminescence is divided into two categories, *fluorescence* and *phosphorescence*, depending on the nature of the excited state.

NOTE: Fluorescence is the emission of electromagnetic radiation light by a substance that has absorbed radiation of a different wavelength. Phosphorescence is a specific type of photoluminescence related to fluorescence. Unlike fluorescence, a phosphorescent material does not immediately re-emit the radiation it absorbs.

The process of fluorescent absorption and emission is easily illustrated by the Jablonski diagram. A classic Jablonski diagram is shown in Figure 3.92, where  $S_n$  represents the  $n^{\text{th}}$  electronic states. There are different vibrational and rotational states in every electronic state. After light absorption, a fluorophore is excited to a higher electronic and vibrational state from ground state (here rotational states are not considered for

<sup>13</sup>This content is available online at <<http://cnx.org/content/m34680/1.1/>>.

simplicity). By internal conversion of energy, these excited molecules relax to lower vibrational states in  $S_1$  (Figure 3.92) and then return to ground states by emitting fluorescence. Actually, excited molecules always return to higher vibration states in  $S_0$  and followed by some thermal process to ground states in  $S_1$ . It is also possible for some molecules to undergo intersystem crossing process to  $T_2$  states (Figure 3.92). After internal conversion and relaxing to  $T_1$ , these molecules can emit phosphorescence and return to ground states.

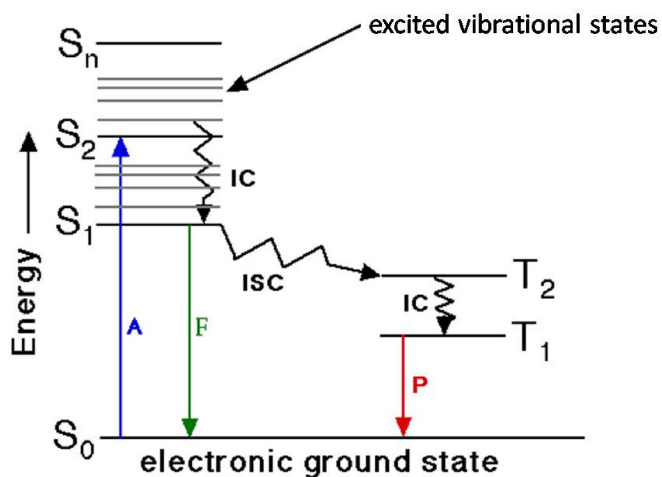


**Figure 3.92:** Jablonski diagram where, A = absorbance, F = fluorescence, P = phosphorescence, S = single state, T = triplet state, IC = internal conversion, ISC = intersystem crossing.

The Stokes shift, the excited state lifetime and quantum yield are the three most important characteristics of fluorescence emission. Stokes shift is the difference between positions of the band maxima of the absorption and emission spectra of the same electronic transition. According to mechanism discussed above, an emission spectrum must have lower energy or longer wavelength than absorption light. The quantum yield is a measure of the intensity of fluorescence, as defined by the ratio of emitted photons over absorbed photons. Excited state lifetime is a measure of the decay times of the fluorescence.

### 3.5.2.2 Instrumentation of Fluorescence Spectroscopy

#### 3.5.2.2.1 Spectrofluorometers

Most spectrofluorometers can record both excitation and emission spectra. An emission spectrum is the wavelength distribution of an emission measured at a single constant excitation wavelength. In comparison, an excitation spectrum is measured at a single emission wavelength by scanning the excitation wavelength.

#### 3.5.2.2.2 Light sources

Specific light sources are chosen depending on the application.

##### 3.5.2.2.2.1 Arc and incandescent xenon lamps

The high-pressure xenon (Xe) arc is the most versatile light source for steady-state fluorometers now. It can provides a steady light output from 250 - 700 nm (Figure 3.93), with only some sharp lines near 450 and 800



nm. The reason that xenon arc lamps emit a continuous light is the recombination of electrons with ionized Xe atoms. These ions produced by collision between Xe and electrons. Those sharp lines near 450 nm are due to the excited Xe atoms that are not ionized.

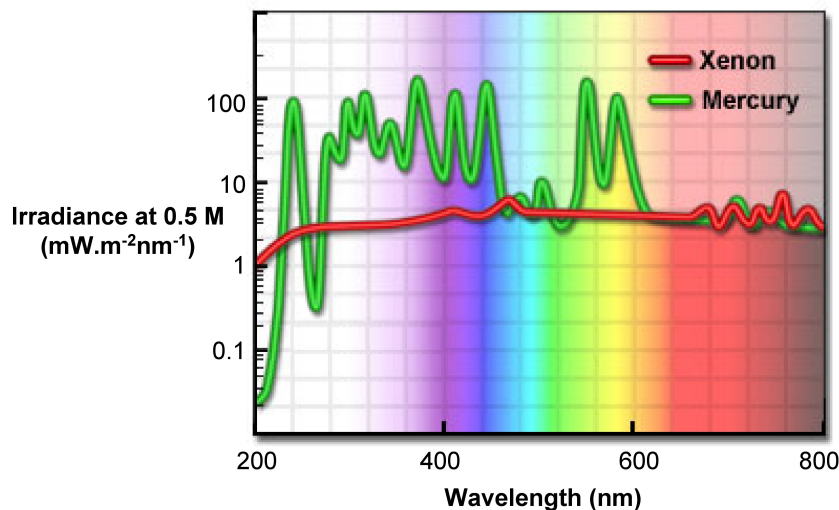


**Figure 3.93:** Spectral irradiance of arc-discharge lamps.

During fluorescence experiment, some distortion of the excitation spectra can be observed, especially the absorbance locating in visible and ultraviolet region. Any distortion displayed in the peaks is the result of wavelength-dependent output of Xe lamps. Therefore, we need to apply some mathematic and physical approaches for correction.

#### 3.5.2.2.2.2 High-pressure mercury (Hg) lamps

Compared with xenon lamps, Hg lamps have higher intensities. As shown in Figure 3.93, the intensity of Hg lamps is concentrated in a series of lines, so it is a potentially better excitation light source if matched to certain fluorophores.

#### 3.5.2.2.2.3 Xe-Hg arc lamps

High-pressure xenon-mercury lamps have been produced. They have much higher intensity in ultraviolet region than normal Xe lamps. Also, the introduction of Xe to Hg lamps broadens the sharp-line output of Hg lamps. Although the wavelength of output is still dominated by those Hg lines, these lines are broadened and fit to various fluorophores better. The Xe-Hg lamp output depends on the operating temperature.

#### 3.5.2.2.2.4 Low pressure Hg and Hg-Ar lamps

Due to their very sharp line spectra, they are primarily useful for calibration purpose. The combination of Hg and Ar improve the output scale, from 200 - 1000 nm.

### 3.5.2.2.2.5 Other light source

There are many other light source for experimental and industrial application, such as pulsed xenon lamps, quartz-tungsten halogen (QTH) lamps, LED light sources, etc.

### 3.5.2.2.3 Monochromators

Most of the light sources used provide only polychromatic or white light. However, what is needed for experiments are various chromatic light with a wavelength range of 10 nm. Monochromators help us to achieve this aim. Prisms and diffraction gratings are the two main kinds of monochromators used, although diffraction gratings are most useful, especially in spectrofluorometers.

Dispersion, efficiency, stray light level and resolution are important parameters for monochromators. Dispersion is mainly determined by slit width and expressed in nm/mm. It is prepared to have low stray light level. Stray light is defined as light transmitted by the monochromator at wavelength outside the chosen range. Also, a high efficiency is required to increase the ability to detect low light levels. Resolution depends on the slit width. There are normally two slits, entrance and exit in a fluorometers. Light intensity that passes through the slits is proportional to the square of the slit width. Larger slits have larger signal levels, but lower resolution, and vice versa. Therefore, it is important to balance the signal intensity and resolution with the slit width.

### 3.5.2.2.4 Optical filters

Optical filters are used in addition to monochromators, because the light passing through monochromator is rarely ideal, optical filters are needed for further purifying light source. If the basic excitation and emission properties of a particular system under study, then selectivity by using optical filters is better than by the use of monochromators. Two kinds of optical filter are gradually employed: colored filters and thin-film filters.

#### 3.5.2.2.4.1 Colored filter

Colored filters are the most traditional filter used before thin-film filter were developed. They can be divided into two categories: monochromatic filter and long-pass filter. The first one only pass a small range of light (about 10 - 25 nm) centered at particular chosen wavelength. In contrast, long pass filter transmit all wavelengths above a particular wavelength. In using these bandpass filters, special attention must be paid to the possibility of emission from the filter itself, because many filters are made up of luminescent materials that are easily excited by UV light. In order to avoid this problem, it is better to set up the filter further away from the sample.

#### 3.5.2.2.4.2 Thin-film filters

The transmission curves of colored class filter are not suitable for some application and as such they are gradually being substituted by thin-film filters. Almost any desired transmission curve can be obtained using a thin film filter.

### 3.5.2.2.5 Detectors

The standard detector used in many spectrofluorometers is the InGaAs array, which can provides rapid and robust spectral characterization in the near-IR. And the liquid-nitrogen cooling is applied to decrease the background noise. Normally, detectors are connected to a controller that can transfer a digital signal to and from the computer.

### 3.5.2.3 Fluorophores

At present a wide range of fluorophores have been developed as fluorescence probes in bio-system. They are widely used for clinical diagnosis, bio-tracking and labeling. The advance of fluorometers has been accompanied with developments in fluorophore chemistry. Thousands of fluorophores have been synthesized, but herein four categories of fluorophores will be discussed with regard their spectral properties and application.

#### 3.5.2.3.1 Intrinsic or natural fluorophores

Tryptophan (trp), tyrosine (tyr), and phenylalanine (phe) are three natural amino acid with strong fluorescence (Figure 3.94). In tryptophan, the indole groups absorbs excitation light as UV region and emit fluorescence.

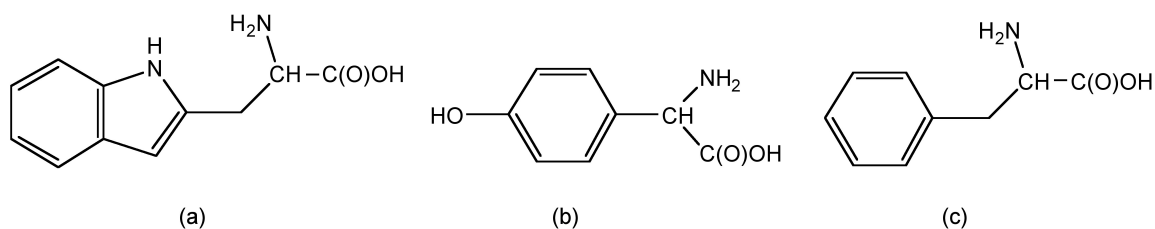


**Figure 3.94:** The structure of (a) tryptophan, (b) tyrosine and (c) phenylalanine.

---

Green fluorescent proteins (GFP) is another natural fluorophores. GFP is composed of 238 amino acids (Figure 3.95), and it exhibits a characteristic bright green fluorescence when excited. They are mainly extracted from bioluminescent jellyfish *Aequorea victoria*, and are employed as signal reporters in molecular biology.

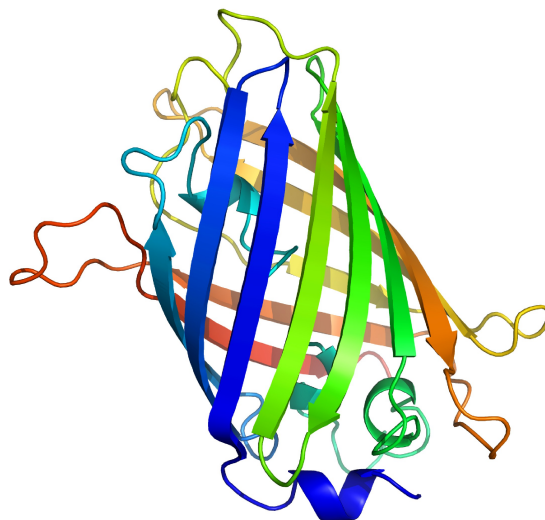


**Figure 3.95:** Green fluorescent proteins (GFP) ribbon diagram.

#### 3.5.2.3.2 Extrinsic fluorophores

Most bio-molecules are nonfluorescent, therefore it is necessary to connect different fluorophores to enable labeling or tracking of the biomolecules. For example, DNA is an example of a biomolecule without fluorescence. The Rhodamine (Figure 3.96) and BODIPY (Figure 3.97) families are two kinds of well-developed organic fluorophores. They have been extensively employed in design of molecular probes due to their excellent photophysical properties.

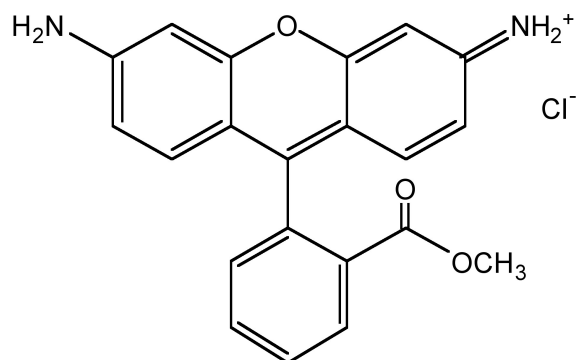


**Figure 3.96:** The structure of Rhodamine 123.

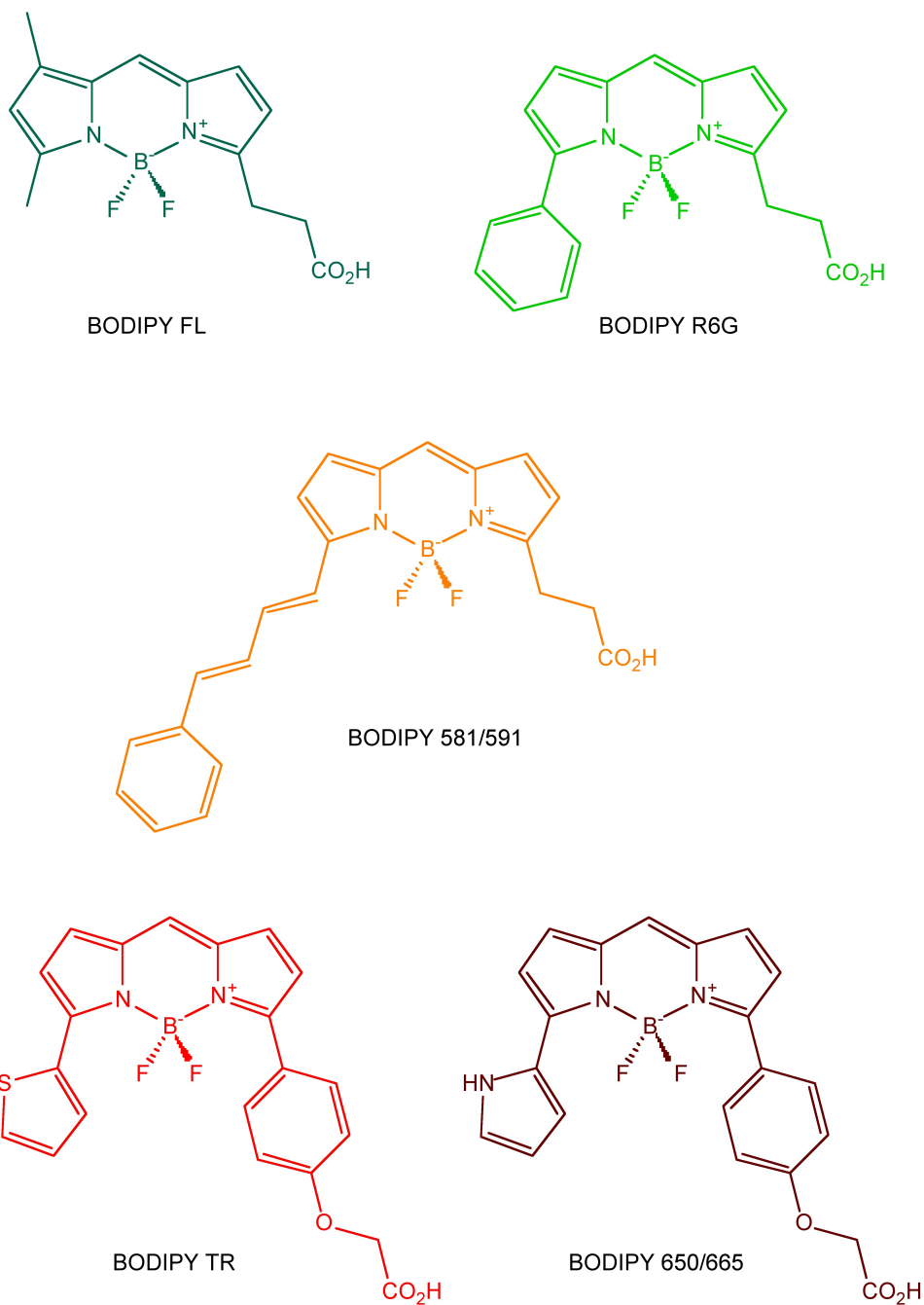


**Figure 3.97:** The structure of selected boron-dipyrromethane (BODIPY) derivatives with their characteristic emission colors.

### 3.5.2.3.3 Red and near-infrared (NIR) dyes

With the development of fluorophores, red and near-infrared (NIR) dyes attract increasing attention since they can improve the sensitivity of fluorescence detection. In biological system, autofluorescence always increase the ratio of signal-to-noise (S/N) and limit the sensitivity. As the excitation wavelength turns to longer, autofluorescence decreases accordingly, and therefore signal-to-noise ratio increases. Cyanines are one such group of long-wavelength dyes, e.g., Cy-3, Cy-5 and Cy-7 (Figure 3.98), which have emission at 555, 655 and 755 nm respectively.

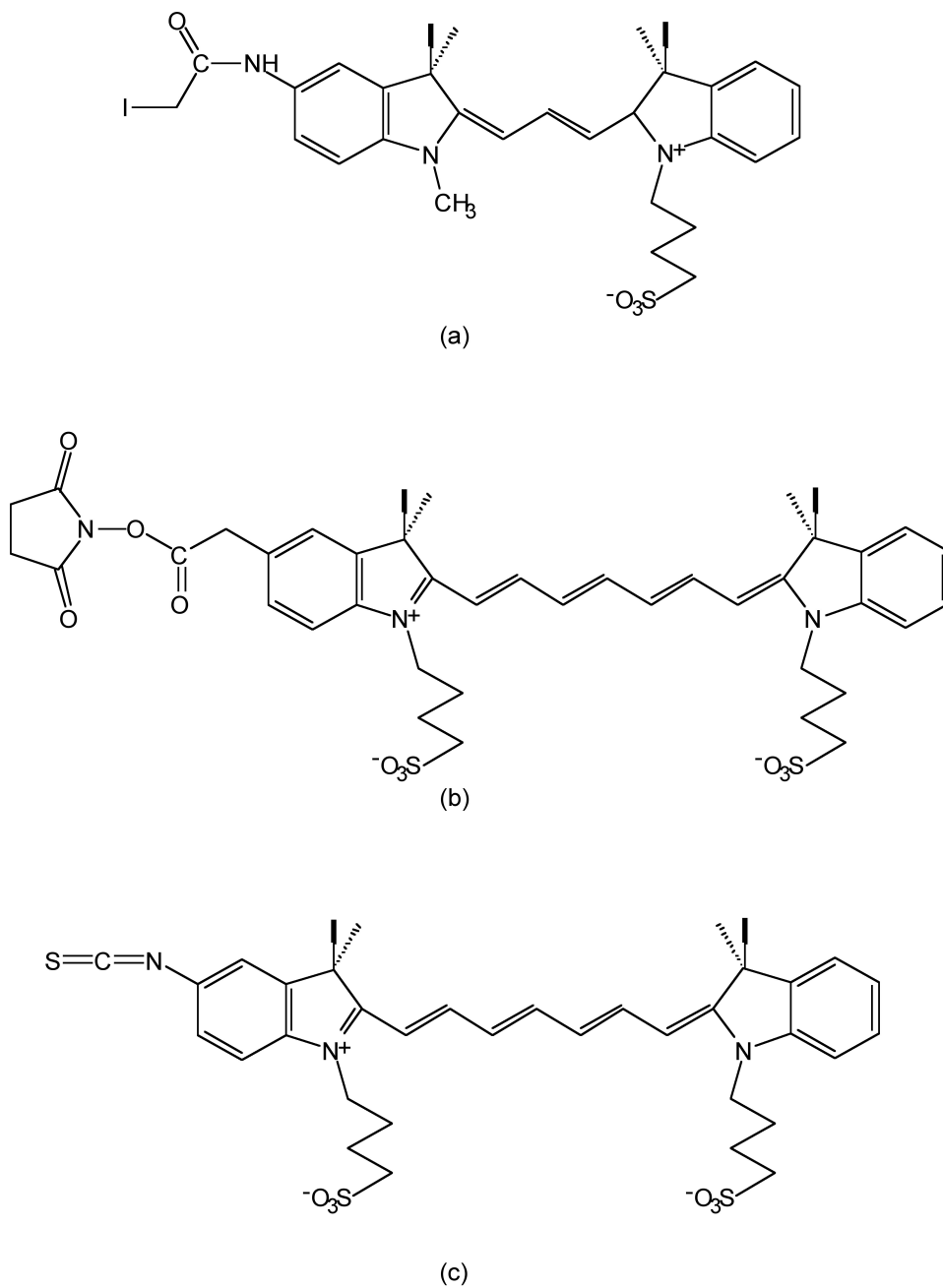


**Figure 3.98:** The structure of (a) Cy-3-iodo acetamide, (b) Cy-5-N-hydroxysuccinimide and (c) Cy-7-isothiocyanate.

### 3.5.2.3.4 Long-lifetime fluorophores

Almost all of the fluorophores mentioned above are organic fluorophores that have relative short lifetime from 1-10 ns. However, there are also a few long-lifetime organic fluorophore, such as pyrene and coronene with lifetime near 400 ns and 200 ns respectively (Figure 3.99). Long-lifetime is one of the important properties to fluorophores. With its help, the autofluorescence in biological system can be removed adequately, and hence improve the detectability over background.

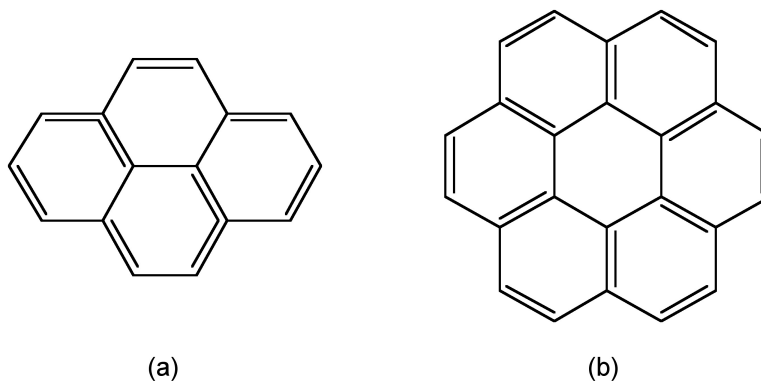


**Figure 3.99:** Structures of (a) pyrene and (b) coronene.

---

Although their emission belongs to phosphorescence, transition metal complexes are a significant class of long-lifetime fluorophores. Ruthenium (II), iridium (III), rhenium (I), and osmium (II) are the most popular transition metals that can combine with one to three diimine ligands to form fluorescent metal complexes. For example, iridium forms a cationic complex with two phenyl pyridine and one diimine ligand (Figure 3.100). This complex has excellent quantum yield and relatively long lifetime.

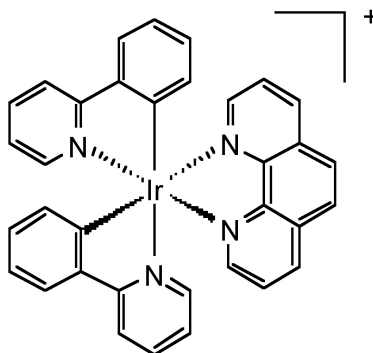


**Figure 3.100:** The structure of the cationic iridium complex,  $(ppy)_2Ir(phen)^+$ .

---



### 3.5.2.4 Applications

With advances in fluorimeters and fluorophores, fluorescence has been a dominant technology in the medical field, such clinic diagnosis and flow cytometry. Herein, the application of fluorescence in DNA and RNA detection is discussed.

The low concentration of DNA and RNA sequences in cells determine that high sensitivity of the probe is required, while the existence of various DNA and RNA with similar structures requires a high selectivity. Hence, fluorophores were introduced as the signal group into probes, because fluorescence spectroscopy is most sensitive technology until now.

The general design of a DNA or RNA probe involves using an antisense hybridization oligonucleotide to monitor target DNA sequence. When the oligonucleotide is connected with the target DNA, the signal groups-the fluorophores-emit designed fluorescence. Based on fluorescence spectroscopy, signal fluorescence can be detected which help us to locate the target DNA sequence. The selectively inherent in the hybridization between two complementary DNA/RNA sequences make this kind of DNA probes extremely high selectivity. A molecular Beacon is one kind of DNA probes. This simple but novel design is reported by Tyagi and Kramer in 1996 (Figure 3.101) and gradually developed to be one of the most common DNA/RNA probes.

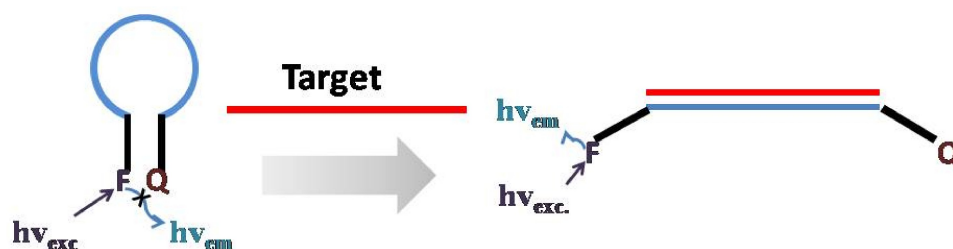


**Figure 3.101:** The structure of molecular beacon and its detecting mechanism.

Generally speaking, a molecular beacon it is composed of three parts: one oligonucleotide, a fluorophore and a quencher at different ends. In the absence of the target DNA, the molecular beacon is folded like a hairpin due to the interaction between the two series nucleotides at opposite ends of the oligonucleotide. At this time, the fluorescence is quenched by the close quencher. However, in the presence of the target, the probe region of the MB will hybridize to the target DNA, open the folded MB and separate the fluorophore and quencher. Therefore, the fluorescent signal can be detected which indicate the existence of a particular DNA.

### 3.5.2.5 Bibliography

- J. R. Lakowicz, *Principles of Fluorescence Spectroscopy*, 3<sup>rd</sup> ed, Springer (2006).
- A. A. Martí, S. Jockusch, N. Stevens, J. Ju, and N. J. Turro, *Acc. Chem. Res.*, 2007, **40**, 402.
- S. Tyagi and F. R. Kramer, *Nat. Biotechnol.*, 1996, **14**, 303.

## 3.6 Mossbauer Spectroscopy

### 3.6.1 Introduction to Mossbauer Spectroscopy<sup>14</sup>

#### 3.6.1.1

In 1957 Rudolf Mossbauer achieved the first experimental observation of the resonant absorption and recoil-free emission of nuclear  $\gamma$ -rays in solids during his graduate work at the Institute for Physics of the Max Planck Institute for Medical Research in Heidelberg Germany. Mossbauer received the 1961 Nobel Prize in Physics for his research in resonant absorption of  $\gamma$ -radiation and the discovery of recoil-free emission a phenomenon that is named after him ([http://nobelprize.org/nobel\\_prizes/physics/laureates/1961](http://nobelprize.org/nobel_prizes/physics/laureates/1961)<sup>15</sup> for more information about Rudolf Mossbauer and his nobel prize). The Mossbauer effect is the basis of Mossbauer spectroscopy.

The Mossbauer effect can be described very simply by looking at the energy involved in the absorption or emission of a  $\gamma$ -ray from a nucleus. When a free nucleus absorbs or emits a  $\gamma$ -ray to conserve momentum the nucleus must recoil, so in terms of energy:

$$E_{\gamma\text{-ray}} = E_{\text{nuclear transition}} - E_{\text{recoil}}$$

When in a solid matrix the recoil energy goes to zero because the effective mass of the nucleus is very large and momentum can be conserved with negligible movement of the nucleus. So, for nuclei in a solid matrix:

$$E_{\gamma\text{-ray}} = E_{\text{nuclear transition}}$$

This is the Mossbauer effect which results in the resonant absorption/emission of  $\gamma$ -rays and gives us a means to probe the hyperfine interactions of an atoms nucleus and its surroundings.

A Mossbauer spectrometer system consists of a  $\gamma$ -ray source that is oscillated toward and away from the sample by a “Mossbauer drive”, a collimator to filter the  $\gamma$ -rays, the sample, and a detector.

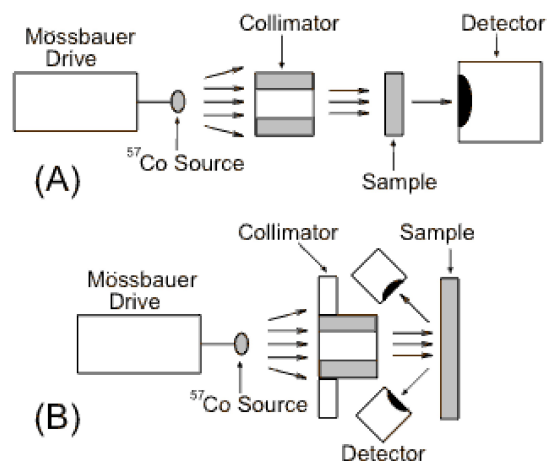


**Figure 3.102:** Schematic of Mossbauer Spectrometers. A = transmission; B = backscatter set up. Adapted from M. D. Dyar, D. G. Agresti, M. W. Schaefer, C. A. Grant, and E. C. Sklute, *Annu. Rev. Earth. Planet. Sci.*, 2006, **34**, 83. Copyright Annual Reviews (2006).

<sup>14</sup>This content is available online at <<http://cnx.org/content/m22328/1.7/>>.

<sup>15</sup>[http://nobelprize.org/nobel\\_prizes/physics/laureates/1961](http://nobelprize.org/nobel_prizes/physics/laureates/1961)

Figure 3.102 shows the two basic set ups for a Mossbauer spectrometer. The Mossbauer drive oscillates the source so that the incident  $\gamma$ -rays hitting the absorber have a range of energies due to the doppler effect. The energy scale for Mossbauer spectra (x-axis) is generally in terms of the velocity of the source in mm/s. The source shown ( $^{57}\text{Co}$ ) is used to probe  $^{57}\text{Fe}$  in iron containing samples because  $^{57}\text{Co}$  decays to  $^{57}\text{Fe}$  emitting a  $\gamma$ -ray of the right energy to be absorbed by  $^{57}\text{Fe}$ . To analyze other Mossbauer isotopes other suitable sources are used. Fe is the most common element examined with Mossbauer spectroscopy because its  $^{57}\text{Fe}$  isotope is abundant enough (2.2), has a low energy  $\gamma$ -ray, and a long lived excited nuclear state which are the requirements for observable Mossbauer spectrum. Other elements that have isotopes with the required parameters for Mossbauer probing are seen in Table 3.13.

Most commonly examined elements	Fe, Ru, W, Ir, Au, Sn, Sb, Te, I, W, Ir, Au, Eu, Gd, Dy, Er, Yb, Np
Elements that exhibit Mossbauer effect	K, Ni, Zn, Ge, Kr, Tc, Ag, Xe, Cs, Ba, La, Hf, Ta, Re, Os, Pt, Hg, Ce, Pr, Nd, Sm, Tb, Ho, Tm, Lu, Th, Pa, U, Pu, Am

**Table 3.13:** Elements with known Mossbauer isotopes and most commonly examined with Mossbauer spectroscopy.

### 3.6.1.1.1 Mossbauer spectra

The primary characteristics looked at in Mossbauer spectra are isomer shift (IS), quadrupole splitting (QS), and magnetic splitting (MS or hyperfine splitting). These characteristics are effects caused by interactions of the absorbing nucleus with its environment.

Isomer shift is due to slightly different nuclear energy levels in the source and absorber due to differences in the s-electron environment of the source and absorber. The oxidation state of an absorber nucleus is one characteristic that can be determined by the IS of a spectra. For example due to greater d electron screening  $\text{Fe}^{2+}$  has less s-electron density than  $\text{Fe}^{3+}$  at its nucleus which results in a greater positive IS for  $\text{Fe}^{2+}$ .

For absorbers with nuclear angular momentum quantum number  $I > \frac{1}{2}$  the non-spherical charge distribution results in quadrupole splitting of the energy states. For example Fe with a transition from  $I=1/2$  to  $3/2$  will exhibit doublets of individual peaks in the Mossbauer spectra due to quadrupole splitting of the nuclear states as shown in red in Figure 3.103.

In the presence of a magnetic field the interaction between the nuclear spin moments with the magnetic field removes all the degeneracy of the energy levels resulting in the splitting of energy levels with nuclear spin  $I$  into  $2I + 1$  sublevels. Using Fe for an example again, magnetic splitting will result in a sextet as shown in green in Figure 3.103. Notice that there are 8 possible transitions shown, but only 6 occur. Due to the selection rule  $\Delta m_I = 0, 1$ , the transitions represented as black arrows do not occur.

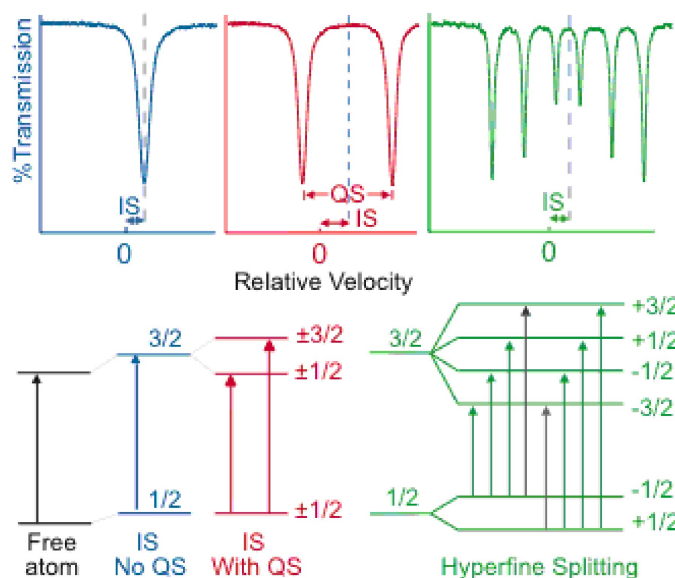


**Figure 3.103:** Characteristics of Mossbauer spectra related to nuclear energy levels. Adapted from M. D. Dyar, D. G. Agresti, M. W. Schaefer, C. A. Grant, and E. C. Sklute, *Annu. Rev. Earth. Planet. Sci.*, 2006, **34**, 83. Copyright Annual Reviews (2006).

### 3.6.1.2 Bibliography

- G. Wertheim. *Mossbauer Effect: Principles and Applications*. New York: Academic Press Inc. (1964).
- D. P. E. Dickson and F. J. Berry. *Mossbauer Spectroscopy*. New York: Cambridge University Press (1986).
- A. G. Maddock. *Mossbauer Spectroscopy: Principles and Applications of the Techniques*. England: Horwood Publishing Limited (1997).
- M. D. Dyar, D. G. Agresti, M. W. Schaefer, C. A. Grant, and E. C. Sklute, *Annu. Rev. Earth. Planet. Sci.*, 2006, **34**, 83.

### 3.6.2 Synthesis of Magnetite Nanoparticles<sup>16</sup>

Numerous schemes have been devised to synthesize magnetite nanoparticles (nMag). The different methods of nMag synthesis can be generally grouped as aqueous or non-aqueous according to the solvents used. Two of the most widely used and explored methods for nMag synthesis are the aqueous co-precipitation method and the non-aqueous thermal decomposition method.

The co-precipitation method of nMag synthesis consists of precipitation of  $\text{Fe}_3\text{O}_4$  (nMag) by addition of a strong base to a solution of  $\text{Fe}^{2+}$  and  $\text{Fe}^{3+}$  salts in water. This method is very simple, inexpensive and produces highly crystalline nMag. The general size of nMag produced by co-precipitation is in the 15 to 50

<sup>16</sup>This content is available online at <<http://cnx.org/content/m22167/1.6/>>.

nm range and can be controlled by reaction conditions, however a large size distribution of nanoparticles is produced by this method. Aggregation of particles is also observed with aqueous methods.

The thermal decomposition method consists of the high temperature thermal decomposition of an iron-oleate complex derived from an iron precursor in the presence of surfactant in a high boiling point organic solvent under an inert atmosphere. For the many variations of this synthetic method many different solvents and surfactants are used. However, in most every method nMag is formed through the thermal decomposition of an iron-oleate complex to form highly crystalline nMag in the 5 to 40 nm range with a very small size distribution. The size of nMag produced is a function of reaction temperature, the iron to surfactant ratio, and the reaction time, and various methods are used that achieve good size control by manipulation of these parameters. The nMag synthesized by organic methods is soluble in organic solvents because the nMag is stabilized by a surfactant surface coating with the polar head group of the surfactant attached to and the hydrophobic tail extending away from the nMag (Figure 3.104). An example of a thermal decomposition method is shown in Figure 3.104.

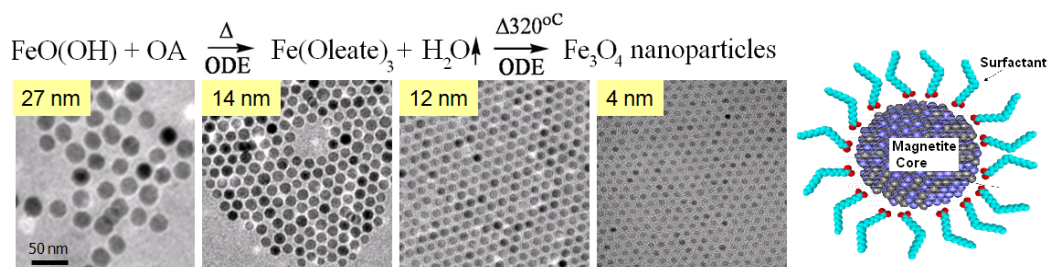


**Figure 3.104:** Top - The reaction equation for this method shows the iron precursor = iron oxo-hydrate, surfactant = oleic acid (OA), and solvent = 1-octadecene. The intermediate iron-oleate complex which thermally decomposes to nMag is formed upon heating the reaction mixture to the 320 °C reaction temperature. Bottom - TEM images showing size control by reaction time (time decreases left to right, constant molar ratio Fe:OA = 1:4 mol, and constant reaction temp T = 320 °C) and small size distribution of nMag. Right - Cartoon of surfactant coated nMag.

### 3.6.2.1 Bibliography

- A. Vioux, *Chem. Mater.* , 1997, **9** , 2292.

## 3.6.3 Mossbauer Analysis of Iron Oxide Nanoparticles<sup>17</sup>

### 3.6.3.1 Spectra and formula calculations

Due to the potential applications of magnetite nanoparticles ( $\text{Fe}_3\text{O}_4$ , nMag) many methods have been devised for its synthesis. However, stoichiometric  $\text{Fe}_3\text{O}_4$  is not always achieved by different synthetic methods. B-site vacancies introduced into the cubic inverse spinel crystal structure of nMag result in nonstoichiometric iron oxide of the formula  $(\text{Fe}^{3+})_A(\text{Fe}_{(1-3x)}^{2+} \text{Fe}_{(1+2x)}^{3+} \text{O}_x)_B\text{O}_4$  where  $\text{O}$  represents B-site vacancy. The magnetic susceptibility which is key to most nMag applications decreases with increased B-site vacancy hence the extent of B-site vacancy is important. The very high sensitivity of the Mossbauer spectrum to the oxidation state and site occupancy of  $\text{Fe}^{3+}$  in cubic inverse spinel iron oxides makes Mossbauer spectroscopy valuable for addressing the issues of whether or not the product of a synthetic method is actually nMag and the extent of B-site vacancy.

<sup>17</sup>This content is available online at <<http://cnx.org/content/m22619/1.3/>>.

As with most analysis using multiple instrumental methods in conjunction is often helpful. This is exemplified by the use of XRD along with Mossbauer spectroscopy in the following analysis. Figure 3.105 shows the XRD results and Mossbauer spectra “magnetite” samples prepared by a  $\text{Fe}^{2+}/\text{Fe}^{3+}$  co-precipitation (Mt025), hematite reduction by hydrogen (MtH2) and hematite reduction with coal (MtC). The XRD analysis shows MtH2 and MT025 exhibiting only magnetite peaks while MtC shows the presence of magnetite, maghemite, and hematite. This information becomes very useful when fitting peaks to the Mossbauer spectra because it gives a chemical basis for peak fitting parameters and helps to fit the peaks correctly.

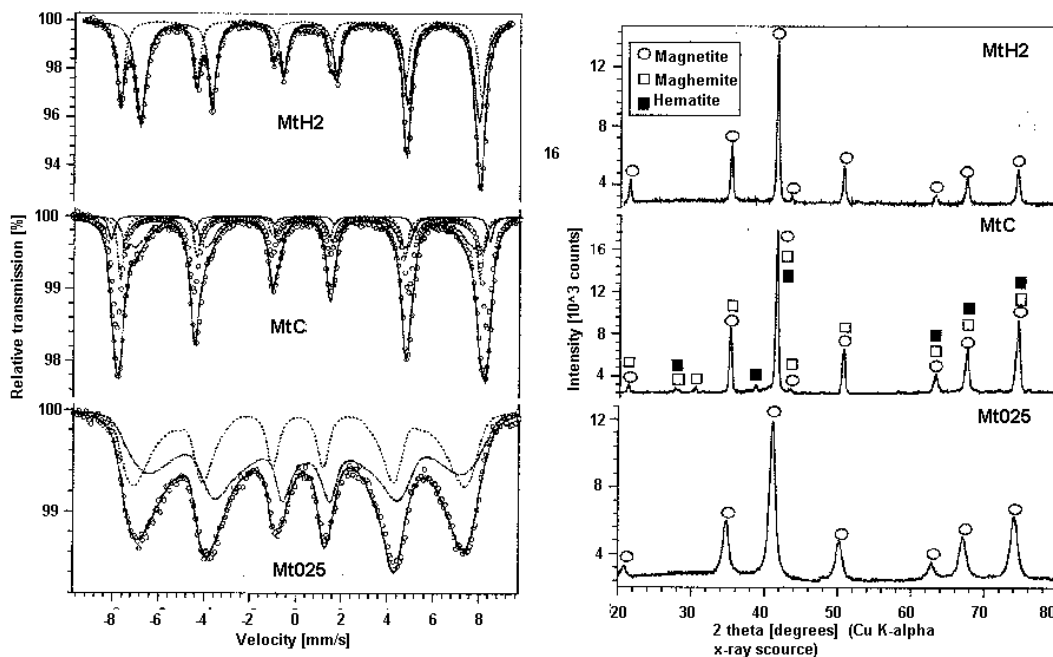


**Figure 3.105:** Mossbauer spectra (left) and corresponding XRD spectra of iron oxide sample prepared by different methods. Adapted from A. L. Andrade, D. M. Souza, M. C. Pereira, J. D. Fabris, and R. Z. Domingues. *J. Nanosci. Nanotechnol.*, 2009, **9**, 2081.

Being that the iron occupies two local environments, the A-site and B site, and two species ( $\text{Fe}^{2+}$  and  $\text{Fe}^{3+}$ ) occupy the B-site one might expect the spectrum to be a combination of 3 spectra, however delocalization of electrons or electron hopping between  $\text{Fe}^{2+}$  and  $\text{Fe}^{3+}$  in the B site causes the nuclei to sense an average valence in the B site thus the spectrum are fitted with two curves accordingly. This is most easily seen in the Mt025 spectrum. The two fitted curves correspond to  $\text{Fe}^{3+}$  in the A-site and mixed valance  $\text{Fe}^{2.5+}$  in the B-site. The isomer shift of the fitted curves can be used to determined which curve corresponds to which valence. The isomer shift relative to the top fitted curve is reported to be 0.661 and the bottom fitted curve is 0.274 relative to  $\alpha\text{Fe}$  thus the top fitted curve corresponds to less s-electron dense  $\text{Fe}^{2.5+}$ . The magnetic splitting is quite apparent. In each of the spectra, six peaks are present due to magnetic splitting of the nuclear energy states as explained previously. Quadrupole splitting is not so apparent, but actually is present in the spectra. The three peaks to the left of the center of a spectrum should be spaced the same as those to the right due to magnetic splitting alone since the energy level spacing between sublevels is equal. This is not the case in the above spectra, because the higher energy  $I = 3/2$  sublevels are split unevenly due

to magnetic and quadrupole splitting interactions.

Once the peaks have been fitted appropriately, determination of the extent of B-site vacancy in  $(\text{Fe}^{3+})_A(\text{Fe}_{(1-3x)}^{2+} \text{Fe}_{(1+2x)}^{3+}\text{O}_x)_B\text{O}_4$  is a relatively simple matter. All one has to do to determine the number of vacancies (x) is solve the equation:

$\frac{RA_B}{RA_A} = \frac{2-6x}{1-5x}$  where  $RA_B$  or  $RA_A$  = relative area ( $\frac{\text{Area A or B site curve}}{\text{Area of both curves}}$ ) of the curve for the B or A site respectively

The reasoning for this equation is as follows. Taking into account that the mixed valance  $\text{Fe}^{2.5+}$  curve is a result of paired interaction between  $\text{Fe}^{2+}$  and  $\text{Fe}^{3+}$  the nonstoichiometric chemical formula is  $(\text{Fe}^{3+})_A(\text{Fe}_{(1-3x)}^{2+} \text{Fe}_{(1+2x)}^{3+}\text{O}_x)_B\text{O}_4$ . The relative intensity (or relative area) of the Fe-A and Fe-B curves is very sensitive to stoichiometry because vacancies in the B-site reduce the Fe-A curve and increase Fe-B curve intensities. This is due to the unpaired  $\text{Fe}_{5x}^{3+}$  adding to the intensity of the Fe-A curve rather than the Fe-B curve. Since the relative area is directly proportional to the number of Fe contributing to the spectrum the ratio of the relative areas is equal to stoichiometric ratio of  $\text{Fe}^{2.5+}$  to  $\text{Fe}^{3+}$ , which yields the above formula.

Example Calculation:

For MtH2  $RA_A/RA_B = 1.89$

Plugging x into the nonstoichiometric iron oxide formula yeilds:

$$\frac{RA_B}{RA_A} = \frac{2-6x}{1-5x} \quad \text{solving for x yeilds} \quad x = \frac{2 - \frac{RA_A}{RA_B}}{5 \frac{RA_A}{RA_B} + 6} = \frac{2-1.89}{5(1.89)+6} = 0.00712$$

$(\text{Fe}^{3+})_A(\text{Fe}_{1.9572}^{2+} \text{Fe}_{0.0356}^{3+})_B\text{O}_4$  (very close to stoichiometric)

Sample	$RA_B/RA_A$	X	Chemical formula
MtH2	1.89	0.007	$(\text{Fe}^{3+})_A(\text{Fe}_{0.979}^{2+} \text{Fe}_{1.014}^{3+})_B\text{O}_4$
MtC	1.66	0.024	$(\text{Fe}^{3+})_A(\text{Fe}_{0.929}^{2+} \text{Fe}_{1.048}^{3+})_B\text{O}_4$
Mt025	1.60	0.029	$(\text{Fe}^{3+})_A(\text{Fe}_{0.914}^{2+} \text{Fe}_{1.057}^{3+})_B\text{O}_4$

**Table 3.14:** Parameters and nonstoichiometric formulas for MtC, Mt025, and MtH2

### 3.6.3.2 Bibliography

- F. C. Voogt, T. Fujii, P. J. M. Smulders, L. Niesen, M. A. James, and T. Hibma, *Phys. Rev. B*, 1999, **60**, 11193.
- A. L. Andrade, D. M. Souza, M. C. Pereira, J. D. Fabris, and R. Z. Domingues, *J. Nanosci. Nanotechnol.*, 2009, **9**, 2081.
- J. B. Yang, X. D. Zhou, W. B. Yelon, W. fJ. James, Q. Cai, K. V. Gopalakrishnan, S. K. Malik, X. C. Sun, and D. E. Nikles, *J. Appl. Phys.*, 2004, **95**, 7540.
- R.E. Vandenberghe, I. Nedkov, T. Merodiiska, and L. Slavov, *Hyperfine Interact.* 2005, **165**, 267.

## 3.6.4 Determining the Chemical Formula of Nonstoichiometric Iron Oxide Nanoparticles by Mossbauer Spectroscopy<sup>18</sup>

### 3.6.4.1 Chemical formula determination

Magnetite ( $\text{Fe}_3\text{O}_4$ ) nanoparticles (n-Mag) are nanometer sized, superparamagnetic, have high saturation magnetization, high magnetic susceptibility, and low toxicity. These properties could be utilized for many

<sup>18</sup>This content is available online at <<http://cnx.org/content/m22184/1.4/>>.

possible applications; hence, n-Mag has attracted much attention in the scientific community. Some of the potential applications include drug delivery, hyperthermia agents, MRI contrast agents, cell labeling, and cell separation to name a few.

The crystal structure of n-Mag is cubic inverse spinel with  $\text{Fe}^{3+}$  cations occupying the interstitial tetrahedral sites(A) and  $\text{Fe}^{3+}$  along with  $\text{Fe}^{2+}$  occupying the interstitial octahedral sites(B) of an FCC lattice of  $\text{O}^{2-}$ . Including the site occupation and charge of Fe, the n-Mag chemical formula can be written  $(\text{Fe}^{3+})_A(\text{Fe}^{2+}\text{Fe}^{3+})_B\text{O}_4$ . Non-stoichiometric iron oxide results from B-site vacancies in the crystal structure. To maintain balanced charge and take into account the degree of B-site vacancies the iron oxide formula is written  $(\text{Fe}^{3+})_A(\text{Fe}_{(1-3x)})^{2+}\text{Fe}_{(1+2x)}^{3+}\text{O}_x)_B\text{O}_4$  where  $\text{O}$  represents B-site vacancy. The extent of B-site vacancy has a significant effect on the magnetic properties of iron oxide and in the synthesis of n-Mag stoichiometric iron oxide is not guaranteed; therefore, B-site vacancy warrants attention in iron oxide characterization, and can be addressed using Mossbauer spectroscopy.

## 3.7 NMR Spectroscopy

### 3.7.1 Introduction to Nuclear Magnetic Resonance Spectroscopy<sup>19</sup>

#### 3.7.1.1 Introduction

Nuclear magnetic resonance spectroscopy (NMR) is a widely used and powerful method that takes advantage of the magnetic properties of certain nuclei. The basic principle behind NMR is that some nuclei exist in specific nuclear spin states when exposed to an external magnetic field. NMR observes transitions between these spin states that are specific to the particular nuclei in question, as well as that nuclei's chemical environment. However, this only applies to nuclei whose spin,  $I$ , is not equal to 0, so nuclei where  $I = 0$  are 'invisible' to NMR spectroscopy. These properties have led to NMR being used to identify molecular structures, monitor reactions, study metabolism in cells, and is used in medicine, biochemistry, physics, industry, and almost every imaginable branch of science.

#### 3.7.1.2 Theory

The chemical theory that underlies NMR spectroscopy depends on the intrinsic spin of the nucleus involved, described by the quantum number  $S$ . Nuclei with a non-zero spin are always associated with a non-zero magnetic moment, as described by (3.8), where  $\mu$  is the magnetic moment,  $S$  is the spin, and  $\gamma$  is always non-zero. It is this magnetic moment that allows for NMR to be used; therefore nuclei whose quantum spin is zero cannot be measured using NMR. Almost all isotopes that have both an even number of protons and neutrons have no magnetic moment, and cannot be measured using NMR.

$$\mu = \gamma.S \quad (3.8)$$

In the presence of an external magnetic field ( $B$ ) for a nuclei with a spin  $I = 1/2$ , there are two spin states present of  $+1/2$  and  $-1/2$ . The difference in energy between these two states at a specific external magnetic field ( $B_x$ ) are given by (3.9), and are shown in Figure 3.106, where  $E$  is energy,  $I$  is the spin of the nuclei, and  $\mu$  is the magnetic moment of the specific nuclei being analyzed. The difference in energy shown is always extremely small, so for NMR strong magnetic fields are required to further separate the two energy states. At the applied magnetic fields used for NMR, most magnetic resonance frequencies tend to fall in the radio frequency range.

$$E = \mu.B_x/I \quad (3.9)$$

<sup>19</sup>This content is available online at <<http://cnx.org/content/m38356/1.1/>>.



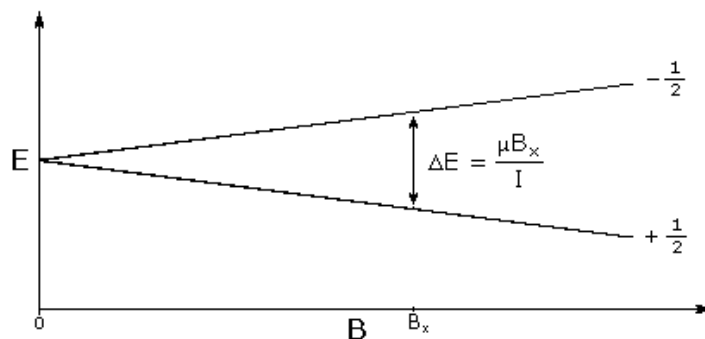


**Figure 3.106:** The difference in energy between two spin states over a varying magnetic field  $B$ .

The reason NMR can differentiate between different elements and isotopes is due to the fact that each specific nuclide will only absorb at a very specific frequency. This specificity means that NMR can generally detect one isotope at a time, and this results in different types of NMR: such as  $^1\text{H}$  NMR,  $^{13}\text{C}$  NMR, and  $^{31}\text{P}$  NMR, to name only a few.

The subsequent absorbed frequency of any type of nuclei is not always constant, since electrons surrounding a nucleus can result in an effect called nuclear shielding, where the magnetic field at the nucleus is changed (usually lowered) because of the surrounding electron environment. This differentiation of a particular nucleus based upon its electronic (chemical) environment allows NMR be used to identify structure. Since nuclei of the same type in different electron environments will be more or less shielded than another, the difference in their environment (as observed by a difference in the surrounding magnetic field) is defined as the chemical shift.

### 3.7.1.3 Instrumentation

An example of an NMR spectrometer is given in Figure 3.107. NMR spectroscopy works by varying the machine's emitted frequency over a small range while the sample is inside a constant magnetic field. Most of the magnets used in NMR machines to create the magnetic field range from 6 to 24 T. The sample is placed within the magnet and surrounded by superconducting coils, and is then subjected to a frequency from the radio wave source. A detector then interprets the results and sends it to the main console.

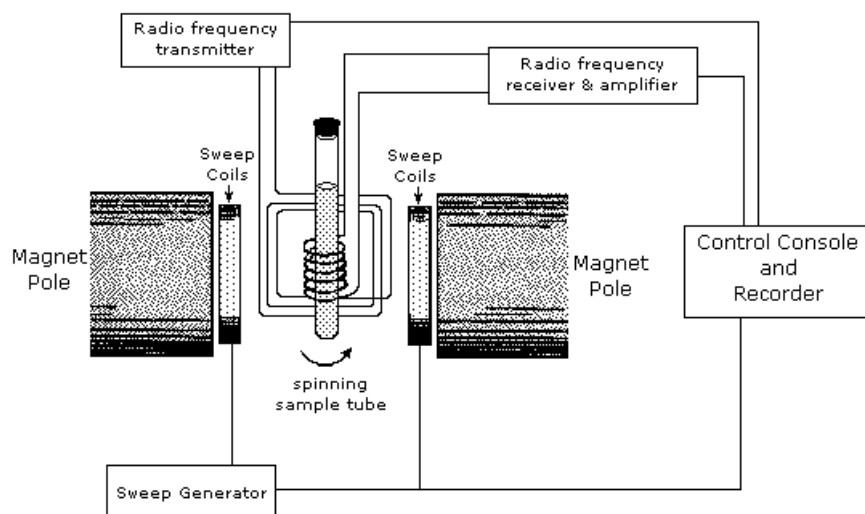


**Figure 3.107:** Diagram of an NMR spectrometer.

### 3.7.1.4 Interpreting NMR spectra

#### 3.7.1.4.1 Chemical shift

The different local chemical environments surrounding any particular nuclei causes them to resonate at slightly different frequencies. This is a result of a nucleus being more or less shielded than another. This is called the chemical shift ( $\delta$ ). One factor that affects chemical shift is the changing of electron density from around a nucleus, such as a bond to an electronegative group. Hydrogen bonding also changes the electron density in  $^1\text{H}$  NMR, causing a larger shift. These frequency shifts are miniscule in comparison to the fundamental NMR frequency differences, on a scale of Hz as compared to MHz. For this reason chemical shifts ( $\delta$ ) are described by the unit ppm on an NMR spectra, (3.10), where  $H_{\text{ref}}$  = the resonance frequency of the reference,  $H_{\text{sub}}$  = resonance frequency of the substance, and  $H_{\text{machine}}$  = operating frequency of the spectrometer.

$$\delta = \left( \frac{H_{\text{ref}} - H_{\text{sub}}}{H_{\text{machine}}} \right) \times 10^6 \quad (3.10)$$

Since the chemical shift ( $\delta$  in ppm) is reported as a relative difference from some reference frequency, so a reference is required. In  $^1\text{H}$  and  $^{13}\text{C}$  NMR, for example, tetramethylsilane (TMS,  $\text{Si}(\text{CH}_3)_4$ ) is used as the reference. Chemical shifts can be used to identify structural properties in a molecule based on our understanding of different chemical environments. Some examples of where different chemical environments fall on a  $^1\text{H}$  NMR spectra are given in Table 3.15.

Functional group	Chemical shift range (ppm)
Alkyl (e.g., methyl -CH <sub>3</sub> )	~ 1
Alkyl adjacent to oxygen (-CH <sub>2</sub> -O)	3 - 4
Alkene (=CH <sub>2</sub> )	~ 6
Alkyne (C-H)	~ 3
Aromatic	7 - 8

**Table 3.15:** Representative chemical shifts for organic groups in the  $^1\text{H}$  NMR.

In Figure 3.108, an  $^1\text{H}$  NMR spectra of ethanol, we can see a clear example of chemical shift. There are three sets of peaks that represent the six hydrogens of ethanol ( $\text{C}_2\text{H}_6\text{O}$ ). The presence of three sets of peaks means that there are three different chemical environments that the hydrogens can be found in: the terminal methyl ( $\text{CH}_3$ ) carbon's three hydrogens, the two hydrogens on the methylene ( $\text{CH}_2$ ) carbon adjacent to the oxygen, and the single hydrogen on the oxygen of the alcohol group ( $\text{OH}$ ). Once we cover spin-spin coupling, we will have the tools available to match these groups of hydrogens to their respective peaks.

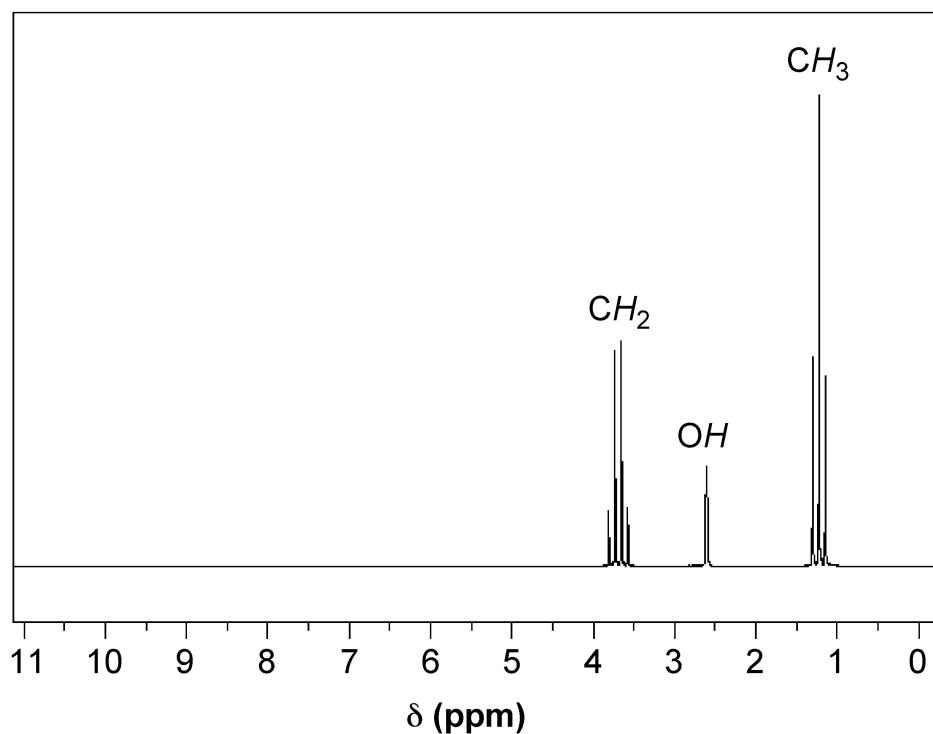


**Figure 3.108:** A  $^1\text{H}$  NMR spectra of ethanol ( $\text{CH}_3\text{CH}_2\text{OH}$ ).

### 3.7.1.4.2 Spin-spin coupling

Another useful property that allows NMR spectra to give structural information is called spin-spin coupling, which is caused by spin coupling between NMR active nuclei that are not chemically identical. Different spin states interact through chemical bonds in a molecule to give rise to this coupling, which occurs when a nuclei being examined is disturbed or influenced by a nearby nuclear spin. In NMR spectra, this effect is shown through peak splitting that can give direct information concerning the connectivity of atoms in a molecule. Nuclei which share the same chemical shift do not form splitting peaks in an NMR spectra.

In general, neighboring NMR active nuclei three or fewer bonds away lead to this splitting. The splitting is described by the relationship where  $n$  neighboring nuclei result in  $n+1$  peaks, and the area distribution can be seen in Pascal's triangle in Figure 3.109. However, being adjacent to a strongly electronegative group such as oxygen can prevent spin-spin coupling. For example a doublet would have two peaks with intensity ratios of 1:1, while a quartet would have four peaks of relative intensities 1:3:3:1. The magnitude of the observed spin splitting depends on many factors and is given by the coupling constant  $J$ , which is in units of Hz.

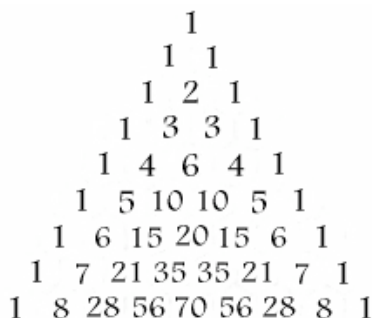


**Figure 3.109:** Pascal's triangle.

---

Referring again to Figure 3.108, we have a good example of how spin-spin coupling manifests itself in an NMR spectra. In the spectra we have three sets of peaks: a quartet, triplet, and a singlet. If we start with the terminal carbon's hydrogens in ethanol, using the  $n+1$  rule we see that they have two hydrogens within three bonds (i.e., H-C-C-H), leading us to identify the triplet as the peaks for the terminal carbon's hydrogens. Looking next at the two central hydrogens, they have four NMR active nuclei within three bonds (i.e., H-C-C-H), but there is no quintet on the spectra as might be expected. This can be explained by the fact that the single hydrogen bonded to the oxygen is shielded from spin-spin coupling, so it must be a singlet and the two central hydrogens form the quartet. We have now interpreted the NMR spectra of ethanol by identifying which nuclei correspond to each peak.

### 3.7.1.4.3 Peak intensity

Mainly useful for proton NMR, the size of the peaks in the NMR spectra can give information concerning the number of nuclei that gave rise to that peak. This is done by measuring the peak's area using integration. Yet even without using integration the size of different peaks can still give relative information about the number of nuclei. For example a singlet associated with three hydrogen atoms would be about 3 times larger than a singlet associated with a single hydrogen atom.

This can also be seen in the example in Figure 3.108. If we integrated the area under each peak, we would find that the ratios of the areas of the quartet, singlet, and triplet are approximately 2:1:3, respectively.

### 3.7.1.5 Limitations of NMR

Despite all of its upsides, there are several limitations that can make NMR analysis difficult or impossible in certain situations. One such issue is that the desired isotope of an element that is needed for NMR analysis may have little or no natural abundance. For example the natural abundance of  $^{13}\text{C}$ , the active isotope for carbon NMR, is about 11%, which works well for analysis. However, in the case of oxygen the active isotope for NMR is  $^{17}\text{O}$ , which is only 0.035% naturally abundant. This means that there are certain elements that can essentially never be measured through NMR.

Another problem is that some elements have an extremely low magnetic moment,  $\mu$ . The sensitivity of NMR machines is based on the magnetic moment of the specific element, but if the magnetic moment is too low it can be very difficult to obtain an NMR spectra with enough peak intensity to properly analyze.

### 3.7.1.6 Bibliography

- D. L. Nelson and M. M. Cox, *Principles of Biochemistry*, 5<sup>th</sup> Ed, W. H. Freeman and Company, New York (2008).
- D. F. Shriver and P. W. Atkins, *Inorganic Chemistry*, 4<sup>th</sup> Ed, Oxford University Press (2006).
- I. C. P. Smith and D. E. Blandford, *Anal. Chem.*, 1995, **67**, 509.

## 3.7.2 NMR Properties of the Elements<sup>20</sup>

Isotope	Natural abundance (%)	Relative NMR frequency (MHz)	Relative receptivity as compared to $^1\text{H}$
$^1\text{H}$	99.985	100	1.00
$^3\text{H}$	-	106.7	-
$^3\text{He}$	0.00013	76.2	$5.8 \times 10^{-7}$
$^{13}\text{C}$	1.11	25.1	$1.8 \times 10^{-4}$
$^{15}\text{N}$	0.37	10.1	$3.9 \times 10^{-6}$
$^{19}\text{F}$	100	94.1	$8.3 \times 10^{-1}$
$^{29}\text{Si}$	4.7	19.9	$3.7 \times 10^{-4}$
$^{31}\text{P}$	100	40.5	$6.6 \times 10^{-2}$
$^{57}\text{Fe}$	2.2	3.2	$7.4 \times 10^{-7}$
$^{77}\text{Se}$	7.6	19.1	$5.3 \times 10^{-4}$
$^{89}\text{Y}$	100	4.9	$1.2 \times 10^{-4}$
$^{103}\text{Rh}$	100	3.2	$3.2 \times 10^{-5}$
$^{107}\text{Ag}$	51.8	4.0	$3.5 \times 10^{-5}$

*continued on next page*

<sup>20</sup>This content is available online at <<http://cnx.org/content/m34632/1.1/>>.

$^{109}\text{Ag}$	48.2	4.7	$4.9 \times 10^{-5}$
$^{111}\text{Cd}$	12.8	21.2	$1.2 \times 10^{-3}$
$^{113}\text{Cd}$	12.3	22.2	$1.3 \times 10^{-3}$
$^{117}\text{Sn}^{\text{a}}$	7.6	35.6	$3.5 \times 10^{-3}$
$^{119}\text{Sn}$	8.6	37.3	$4.5 \times 10^{-3}$
$^{125}\text{Te}^{\text{a}}$	7.0	31.5	$2.2 \times 10^{-3}$
$^{129}\text{Xe}$	26.4	27.8	$5.7 \times 10^{-3}$
$^{169}\text{Tm}$	100	8.3	$5.7 \times 10^{-4}$
$^{171}\text{Yb}$	14.3	17.6	$7.8 \times 10^{-4}$
$^{183}\text{W}$	14.4	4.2	$1.1 \times 10^{-5}$
$^{187}\text{Os}$	1.6	2.3	$2.0 \times 10^{-7}$
$^{195}\text{Pt}$	33.8	21.4	$3.4 \times 10^{-3}$
$^{199}\text{Hg}$	16.8	17.9	$9.8 \times 10^{-4}$
$^{203}\text{Tl}$	29.5	57.1	$5.7 \times 10^{-2}$
$^{205}\text{Tl}$	70.5	57.6	$1.4 \times 10^{-1}$
$^{207}\text{Pb}$	22.6	20.9	$2.0 \times 10^{-1}$

**Table 3.16:** NMR properties of selected spin  $1/2$  nuclei. <sup>a</sup> Other spin  $1/2$  also exist.

Isotope	Spin	Natural abundance (%)	Relative NMR frequency (MHz)	Relative receptivity as compared to $^1\text{H}$	Quadrupole moment ( $10^{-28} \text{ m}^2$ )
$^2\text{H}$	1	0.015	15.4	$1.5 \times 10^{-6}$	$2.8 \times 10^{-3}$
$^6\text{Li}$	1	7.4	14.7	$6.3 \times 10^{-4}$	$-8 \times 10^{-4}$
$^7\text{Li}$	$3/2$	92.6	38.9	$2.7 \times 10^{-1}$	$-4 \times 10^{-2}$
$^9\text{Be}$	$3/2$	100	14.1	$1.4 \times 10^{-2}$	$5 \times 10^{-2}$
$^{10}\text{B}$	3	19.6	10.7	$3.9 \times 10^{-3}$	$8.5 \times 10^{-2}$
$^{11}\text{B}$	$3/2$	80.4	32.1	$1.3 \times 10^{-1}$	$4.1 \times 10^{-2}$
$^{14}\text{Na}$	1	99.6	7.2	$1.0 \times 10^{-3}$	$1 \times 10^{-2}$
$^{17}\text{O}$	$5/2$	0.037	13.6	$1.1 \times 10^{-5}$	$-2.6 \times 10^{-2}$
$^{23}\text{Na}$	$5/2$	100	26.5	$9.3 \times 10^{-2}$	$1 \times 10^{-1}$
<i>continued on next page</i>					

$^{25}\text{Mg}$	$5/2$	10.1	6.1	$2.7 \times 10^{-4}$	$2.2 \times 10^{-1}$
$^{27}\text{Al}$	$5/2$	100	26.1	$2.1 \times 10^{-1}$	$1.5 \times 10^{-1}$
$^{33}\text{S}$	$3/2$	0.76	7.7	$1.7 \times 10^{-5}$	$-5.5 \times 10^{-2}$
$^{35}\text{Cl}$	$3/2$	75.5	9.8	$3.6 \times 10^{-3}$	$-1 \times 10^{-1}$
$^{37}\text{Cl}$	$3/2$	24.5	8.2	$6.7 \times 10^{-4}$	$-7.9 \times 10^{-2}$
$^{39}\text{K}^b$	$3/2$	93.1	4.7	$4.8 \times 10^{-4}$	$4.9 \times 10^{-2}$
$^{43}\text{Ca}$	$7/2$	0.15	6.7	$8.7 \times 10^{-6}$	$2 \times 10^{-1}$
$^{45}\text{Sc}$	$7/2$	100	24.3	$3.0 \times 10^{-1}$	$-2.2 \times 10^{-1}$
$^{47}\text{Ti}$	$5/2$	7.3	5.6	$1.5 \times 10^{-4}$	$2.9 \times 10^{-1}$
$^{49}\text{Ti}$	$7/2$	5.5	5.6	$2.1 \times 10^{-4}$	$2.4 \times 10^{-1}$
$^{51}\text{V}^b$	$7/2$	99.8	26.3	$3.8 \times 10^{-1}$	$-5 \times 10^{-2}$
$^{53}\text{Cr}$	$3/2$	9.6	5.7	$8.6 \times 10^{-5}$	$3 \times 10^{-2}$
$^{55}\text{Mn}$	$5/2$	100	24.7	$1.8 \times 10^{-1}$	$4 \times 10^{-1}$
$^{59}\text{Co}$	$7/2$	100	23.6	$2.8 \times 10^{-1}$	$3.8 \times 10^{-1}$
$^{61}\text{Ni}$	$3/2$	1.2	8.9	$4.1 \times 10^{-1}$	$1.6 \times 10^{-1}$
$^{63}\text{Cu}$	$3/2$	69.1	26.5	$6.5 \times 10^{-2}$	$-2.1 \times 10^{-1}$
$^{65}\text{Cu}$	$3/2$	30.9	28.4	$3.6 \times 10^{-2}$	$-2.0 \times 10^{-1}$
$^{67}\text{Zn}$	$5/2$	4.1	6.3	$1.2 \times 10^{-4}$	$1.6 \times 10^{-1}$
$^{69}\text{Ga}$	$3/2$	60.4	24.0	$4.2 \times 10^{-2}$	$1.9 \times 10^{-1}$
$^{71}\text{Ga}$	$3/2$	39.6	30.6	$5.7 \times 10^{-2}$	$1.2 \times 10^{-1}$
$^{73}\text{Ge}$	$9/2$	7.8	3.5	$1.1 \times 10^{-4}$	$-1.8 \times 10^{-1}$
$^{75}\text{As}$	$3/2$	100	17.2	$2.5 \times 10^{-2}$	$2.9 \times 10^{-1}$
$^{79}\text{Br}$	$3/2$	50.5	25.1	$4.0 \times 10^{-2}$	$3.7 \times 10^{-1}$
$^{81}\text{Br}$	$3/2$	49.5	27.1	$4.9 \times 10^{-2}$	$3.1 \times 10^{-1}$
$^{87}\text{Rb}^b$	$3/2$	27.9	32.8	$4.9 \times 10^{-2}$	$1.3 \times 10^{-1}$
$^{87}\text{Sr}$	$9/2$	7.0	4.3	$1.9 \times 10^{-4}$	$3 \times 10^{-1}$
$^{91}\text{Zr}$	$5/2$	11.2	9.3	$1.1 \times 10^{-3}$	$-2.1 \times 10^{-1}$
$^{93}\text{Nb}$	$9/2$	100	24.5	$4.9 \times 10^{-1}$	$-2.2 \times 10^{-1}$
<i>continued on next page</i>					

<sup>95</sup> Mo	$5/2$	15.7	6.5	$5.1 \times 10^{-4}$	$\pm 1.2 \times 10^{-1}$
<sup>97</sup> Mo	$5/2$	9.5	6.7	$3.3 \times 10^{-4}$	$\pm 1.1$
<sup>99</sup> Ru	$5/2$	12.7	4.6	$1.5 \times 10^{-4}$	$7.6 \times 10^{-2}$
<sup>101</sup> Ru	$5/2$	17.1	5.2	$2.8 \times 10^{-4}$	$4.4 \times 10^{-1}$
<sup>105</sup> Pd	$5/2$	22.2	4.6	$2.5 \times 10^{-4}$	$8 \times 10^{-1}$
<sup>115</sup> In <sup>b</sup>	$9/2$	95.7	22.0	$3.4 \times 10^{-1}$	$8.3 \times 10^{-1}$
<sup>121</sup> Sb	$5/2$	57.3	24.0	$9.3 \times 10^{-2}$	$-2.8 \times 10^{-1}$
<sup>123</sup> Sb	$7/2$	42.7	13.0	$2.0 \times 10^{-2}$	$-3.6 \times 10^{-1}$
<sup>127</sup> I	$5/2$	100	20.1	$9.5 \times 10^{-2}$	$-7.9 \times 10^{-1}$
<sup>131</sup> Xe <sup>a</sup>	$3/2$	21.3	8.2	$5.9 \times 10^{-4}$	$-1.2 \times 10^{-1}$
<sup>133</sup> Cs	$7/2$	100	13.2	$4.8 \times 10^{-2}$	$-3 \times 10^{-3}$
<sup>137</sup> Ba <sup>b</sup>	$3/2$	11.3	11.1	$7.9 \times 10^{-4}$	$2.8 \times 10^{-1}$
<sup>139</sup> La	$7/2$	99.9	14.2	$6.0 \times 10^{-2}$	$2.2 \times 10^{-1}$
<sup>177</sup> Hf	$7/2$	18.5	4.0	$2.6 \times 10^{-4}$	4.5
<sup>179</sup> Hf	$9/2$	13.8	2.5	$7.4 \times 10^{-5}$	5.1
<sup>181</sup> Ta	$7/2$	99.99	12.0	$3.7 \times 10^{-2}$	3
<sup>185</sup> Re	$5/2$	37.1	22.7	$5.1 \times 10^{-2}$	2.3
<sup>187</sup> Re	$5/2$	62.9	22.9	$8.8 \times 10^{-2}$	2.2
<sup>189</sup> Os <sup>a</sup>	$3/2$	16.1	7.8	$3.9 \times 10^{-4}$	$8 \times 10^{-1}$
<sup>191</sup> Ir	$3/2$	37.3	1.7	$9.8 \times 10^{-6}$	1.1
<sup>193</sup> Ir	$3/2$	62.7	1.9	$2.1 \times 10^{-5}$	1.0
<sup>197</sup> Au	$3/2$	100	1.7	$2.6 \times 10^{-5}$	$5.9 \times 10^{-1}$
<sup>201</sup> Hg	$3/2$	13.2	6.6	$1.9 \times 10^{-4}$	$4.4 \times 10^{-1}$
<sup>209</sup> Bi	$9/2$	100	16.2	$1.4 \times 10^{-1}$	$-3.8 \times 10^{-1}$

**Table 3.17:** NMR properties of selected quadrupolar nuclei. <sup>a</sup> A spin  $1/2$  isotope also exists. <sup>b</sup> Other quadrupolar nuclei exist.

### 3.7.3 NMR Spin Coupling<sup>21</sup>

#### 3.7.3.1 The basis of spin coupling

Nuclear magnetic resonance (NMR) signals arise when nuclei absorb a certain radio frequency and are excited from one spin state to another. The exact frequency of electromagnetic radiation that the nucleus absorbs depends on the magnetic environment around the nucleus. This magnetic environment is controlled mostly by the applied field, but is also affected by the magnetic moments of nearby nuclei. Nuclei can be in one of many spin states (Figure 3.110), giving rise to several possible magnetic environments for the observed nucleus to resonate in. This causes the NMR signal for a nucleus to show up as a multiplet rather than a single peak.

<sup>21</sup>This content is available online at <<http://cnx.org/content/m43551/1.1/>>.



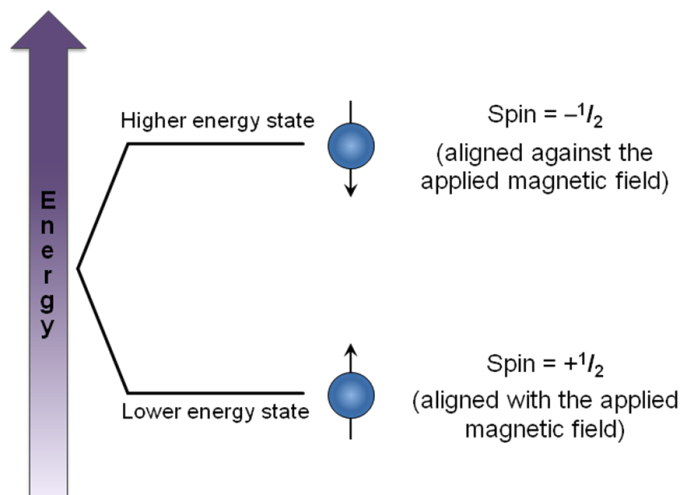


**Figure 3.110:** The different spin states of a nucleus ( $I = 1/2$ ) in a magnetic field. These different states increase or decrease the effective magnetic field experienced by a nearby nucleus, allowing for two distinct signals.

When nuclei have a spin of  $I = 1/2$  (as with protons), they can have two possible magnetic moments and thus split a single expected NMR signal into two signals. When more than one nucleus affects the magnetic environment of the nucleus being examined, complex multiplets form as each nucleus splits the signal into two additional peaks. If those nuclei are magnetically equivalent to each other, then some of the signals overlap to form peaks with different relative intensities. The multiplet pattern can be predicted by Pascal's triangle (Figure 3.111), looking at the  $n^{\text{th}}$  row, where  $n$  = number of nuclei equivalent to each other but *not* equivalent to the one being examined. In this case, the number of peaks in the multiplet is equal to  $n + 1$

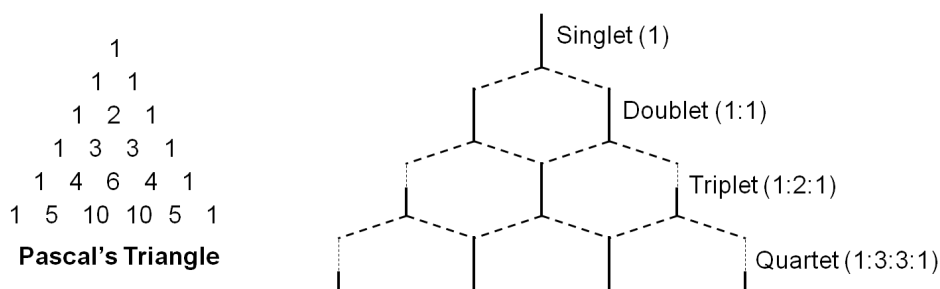


**Figure 3.111:** Pascal's triangle predicts the number of peaks in a multiplet and their relative intensities.

When there is more than one type of nucleus splitting an NMR signal, then the signal changes from a multiplet to a group of multiplets (Figure 3.112). This is caused by the different *coupling constants* associated with different types of nuclei. Each nucleus splits the NMR signal by a different width, so the

peaks no longer overlap to form peaks with different relative intensities.

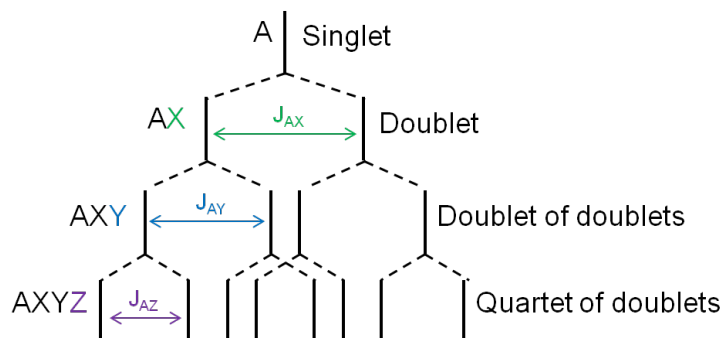


**Figure 3.112:** The splitting tree of different types of multiplets.

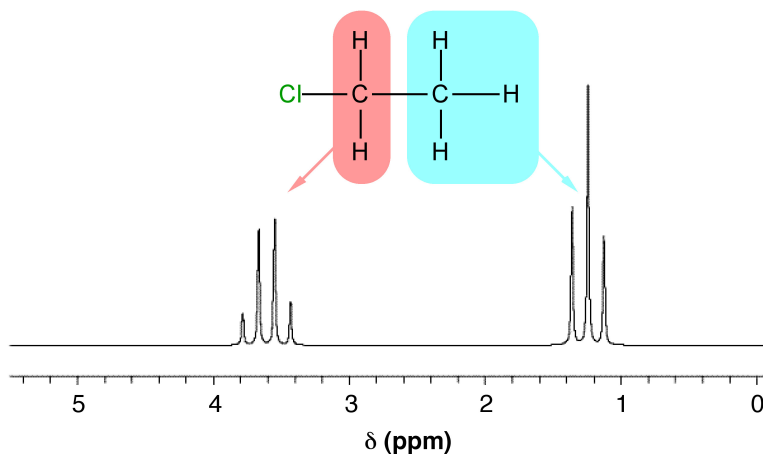
When nuclei have  $I > 1/2$ , they have more than two possible magnetic moments and thus split NMR signals into more than two peaks. The number of peaks expected is  $2I + 1$ , corresponding to the number of possible orientations of the magnetic moment. In reality however, some of these peaks may be obscured due to quadrupolar relaxation. As a result, most NMR focuses on  $I = 1/2$  nuclei such as  $^1\text{H}$ ,  $^{13}\text{C}$ , and  $^{31}\text{P}$ .

Multiplets are centered around the chemical shift expected for a nucleus had its signal not been split. The total area of a multiplet corresponds to the number of nuclei resonating at the given frequency.

### 3.7.3.2 Spin coupling in molecules

Looking at actual molecules raises questions about which nuclei can cause splitting to occur. First of all, it is important to realize that only nuclei with  $I \neq 0$  will show up in an NMR spectrum. When  $I = 0$ , there is only one possible spin state and obviously the nucleus cannot flip between states. Since the NMR signal is based on the absorption of radio frequency as a nucleus transitions from one spin state to another,  $I = 0$  nuclei do not show up on NMR. In addition, they do not cause splitting of other NMR signals because they only have one possible magnetic moment. This simplifies NMR spectra, in particular of organic and organometallic compounds, greatly, since the majority of carbon atoms are  $^{12}\text{C}$ , which have  $I = 0$ .

For a nucleus to cause splitting, it must be close enough to the nucleus being observed to affect its magnetic environment. The splitting technically occurs through bonds, not through space, so as a general rule, only nuclei separated by three or fewer bonds can split each other. However, even if a nucleus is close enough to another, it may not cause splitting. For splitting to occur, the nuclei must also be non-equivalent. To see how these factors affect real NMR spectra, consider the spectrum for chloroethane (Figure 3.113)

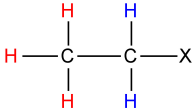
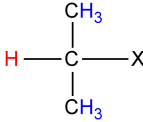
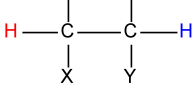
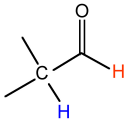
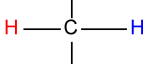
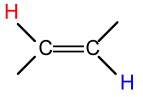
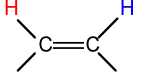
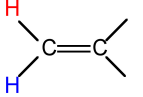
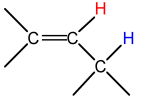
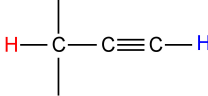
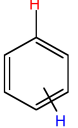


**Figure 3.113:** The NMR spectrum for chloroethane. Adapted from A. M. Castillo, L. Patiny, and J. Wist. *J. Magn. Reson.*, 2010, **209**, 123.

Notice that in Figure 3.113 there are two groups of peaks in the spectrum for chloroethane, a triplet and a quartet. These arise from the two different types of  $I \neq 0$  nuclei in the molecule, the protons on the methyl and methylene groups. The multiplet corresponding to the  $\text{CH}_3$  protons has a relative integration (peak area) of three (one for each proton) and is split by the two methylene protons ( $n = 2$ ), which results in  $n + 1$  peaks, i.e., 3 which is a triplet. The multiplet corresponding to the  $\text{CH}_2$  protons has an integration of two (one for each proton) and is split by the three methyl protons ( $n = 3$ ) which results in  $n + 1$  peaks, i.e., 4 which is a quartet. Each group of nuclei splits the other, so in this way, they are *coupled*.

### 3.7.3.3 Coupling constants

The difference (in Hz) between the peaks of a multiplet is called the *coupling constant*. It is particular to the types of nuclei that give rise to the multiplet, and is independent of the field strength of the NMR instrument used. For this reason, the coupling constant is given in Hz, not ppm. The coupling constant for many common pairs of nuclei are known (Table 3.18), and this can help when interpreting spectra.

Structural type	Coupling constant (Hz)
	6 - 8
	5 - 7
	2 - 12
	0.5 - 3
	12 - 15
	12 - 18
	7 - 12
	0.5 - 3
	3 - 11
	2 - 3
	<i>ortho</i> = 6 - 9; <i>meta</i> = 1 - 3; <i>para</i> = 0 - 1

**Table 3.18:** Typical coupling constants for various organic structural types.

Coupling constants are sometimes written  $^nJ$  to denote the number of bonds ( $n$ ) between the coupled nuclei. Alternatively, they are written as  $J(\text{H-H})$  or  $J_{\text{HH}}$  to indicate the coupling is between two hydrogen atoms. Thus, a coupling constant between a phosphorous atom and a hydrogen would be written as  $J(\text{P-H})$  or  $J_{\text{PH}}$ . Coupling constants are calculated empirically by measuring the distance between the peaks of a multiplet, and are expressed in Hz.

**Example 3.1**

Coupling constants may be calculated from spectra using frequency or chemical shift data. Consider the spectrum of chloroethane shown in Figure 3.114 and the frequency of the peaks (collected on a 60 MHz spectrometer) given in Table 3.19.

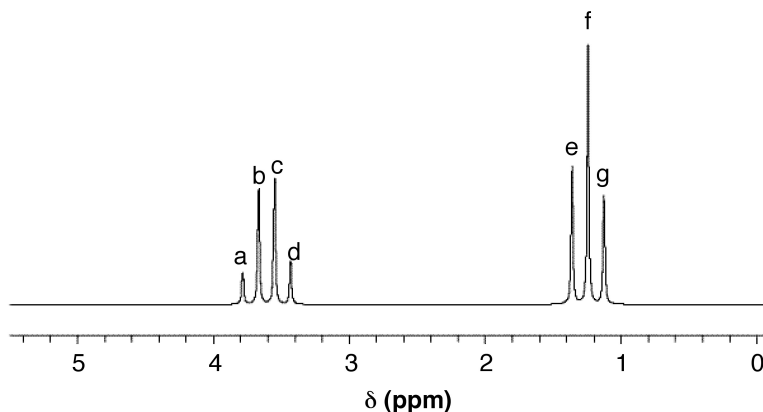


**Figure 3.114:**  $^1\text{H}$  NMR spectrum of chloroethane. Peak positions for labeled peaks are given in Table 3.19.

Peak label	$\delta$ (ppm)	$\nu$ (Hz)
a	3.7805	226.83
b	3.6628	219.77
c	3.5452	212.71
d	3.4275	205.65
e	1.3646	81.88
f	1.2470	74.82
g	1.1293	67.76

**Table 3.19:** Chemical shift in ppm and Hz for all peaks in the  $^1\text{H}$  NMR spectrum of chloroethane. Peak labels are given in Figure 3.114.

To determine the coupling constant for a multiplet (in this case, the quartet in Figure 3.114), the difference in frequency ( $\nu$ ) between each peak is calculated and the average of this value provides the coupling constant in Hz. For example using the data from Table 3.19:

Frequency of peak c - frequency of peak d =  $212.71 \text{ Hz} - 205.65 \text{ Hz} = 7.06 \text{ Hz}$

Frequency of peak b - frequency of peak c =  $219.77 \text{ Hz} - 212.71 \text{ Hz} = 7.06 \text{ Hz}$

Frequency of peak a - frequency of peak b =  $226.83 \text{ Hz} - 219.77 \text{ Hz} = 7.06 \text{ Hz}$

Average: 7.06 Hz

$\therefore J(\text{H-H}) = 7.06 \text{ Hz}$

NOTE: In this case the difference in frequency between each set of peaks is the same and therefore an average determination is not strictly necessary. In fact for 1<sup>st</sup> order spectra they should be the same. However, in some cases the peak picking programs used will result in small variations, and thus it is necessary to take the trouble to calculate a true average.

To determine the coupling constant of the same multiplet using chemical shift data ( $\delta$ ), calculate the difference in ppm between each peak and average the values. Then multiply the chemical shift by the spectrometer field strength (in this case 60 MHz), in order to convert the value from ppm to Hz:

Chemical shift of peak c - chemical shift of peak d = 3.5452 ppm - 3.4275 ppm = 0.1177 ppm

Chemical shift of peak b - chemical shift of peak c = 3.6628 ppm - 3.5452 ppm = 0.1176 ppm

Chemical shift of peak a - chemical shift of peak b = 3.7805 ppm - 3.6628 ppm = 0.1177 ppm

Average: 0.1176 ppm

Average difference in ppm x frequency of the NMR spectrometer = 0.1176 ppm x 60 MHz = 7.056 Hz

$\therefore J(\text{H-H}) = 7.06 \text{ Hz}$

#### Exercise 3.7.3.1

(Solution on p. 416.)

Calculate the coupling constant for triplet in the spectrum for chloroethane (Figure 3.114) using the data from Table 3.19.

#### 3.7.3.4 Second-order coupling

When coupled nuclei have similar chemical shifts (more specifically, when  $\Delta\nu$  is similar in magnitude to  $J$ ), *second-order coupling* or *strong coupling* can occur. In its most basic form, second-order coupling results in “roofing” (Figure 3.115). The coupled multiplets point to or lean toward each other, and the effect becomes more noticeable as  $\Delta\nu$  decreases. The multiplets also become off-centered with second-order coupling. The midpoint between the peaks no longer corresponds exactly to the chemical shift.

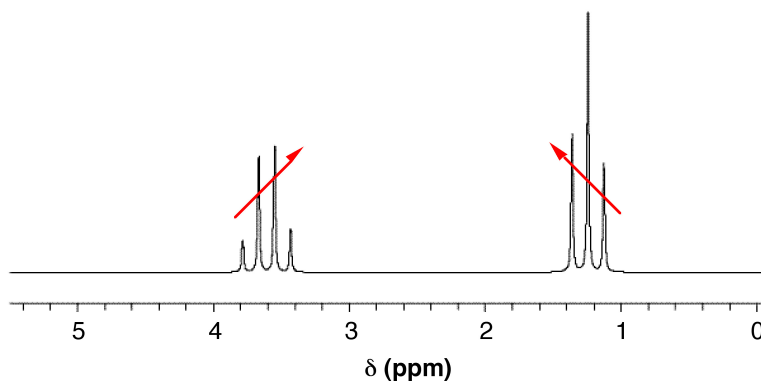


**Figure 3.115:** Roofing can be seen in the NMR spectrum of chloroethane. Adapted from A. M. Castillo, L. Patiny, and J. Wist, *J. Magn. Reson.*, 2010, **209**, 123.

In more drastic cases of strong coupling (when  $\Delta\nu \approx J$ ), multiplets can merge to create deceptively simple patterns. Or, if more than two spins are involved, entirely new peaks can appear, making it difficult to interpret the spectrum manually. Second-order coupling can often be converted into first-order coupling by using a spectrometer with a higher field strength. This works by altering the  $\Delta\nu$  (which is dependent on the field strength), while  $J$  (which is independent of the field strength) stays the same.

### 3.7.3.5 Bibliography

- E. D. Becker, *High Resolution NMR: Theory and Chemical Applications*, 3<sup>rd</sup> ed., Academic Press, San Diego (2000).
- A. M. Castillo, L. Patiny, and J. Wist, *J. Magn. Reson.*, 2010, **209**, 123.
- H. Günther, *NMR Spectroscopy*, 2<sup>nd</sup> ed., John Wiley & Sons Inc., New York (1994).
- P. J. Hore, *Nuclear Magnetic Resonance*, Oxford University Press Inc., New York (1995).
- N. E. Jacobsen, *NMR Spectroscopy Explained: Simplified Theory, Applications and Examples for Organic Chemistry and Structural Biology*, John Wiley & Sons Inc., Hoboken, New Jersey (2007).
- J. Keeler, *Understanding NMR Spectroscopy*, John Wiley & Sons Inc., Hoboken, New Jersey (2005).

## 3.7.4 P-31 NMR Spectroscopy<sup>22</sup>

### 3.7.4.1 Introduction

Phosphorus-31 nuclear magnetic resonance (<sup>31</sup>P NMR) is conceptually the same as proton (<sup>1</sup>H) NMR. The <sup>31</sup>P nucleus is useful in NMR spectroscopy due to its relatively high gyromagnetic ratio (17.235 MHz T<sup>-1</sup>). For comparison, the gyromagnetic ratios of <sup>1</sup>H and <sup>13</sup>C are (42.576 MHz T<sup>-1</sup>) and (10.705 MHz T<sup>-1</sup>), respectively. Furthermore, <sup>31</sup>P has a 100% natural isotopic abundance. Like the <sup>1</sup>H nucleus, the <sup>31</sup>P nucleus has a nuclear spin of 1/2 which makes spectra relatively easy to interpret. <sup>31</sup>P NMR is an excellent technique for studying phosphorus containing compounds, such as organic compounds and metal coordination complexes.

### 3.7.4.2 Differences between <sup>1</sup>H and <sup>31</sup>P NMR

There are certain significant differences between <sup>1</sup>H and <sup>31</sup>P NMR. While <sup>1</sup>H NMR spectra is referenced to tetramethylsilane [Si(CH<sub>3</sub>)<sub>4</sub>], the chemical shifts in <sup>31</sup>P NMR are typically reported relative to 85% phosphoric acid ( $\delta = 0$  ppm), which is used as an external standard due to its reactivity. However, trimethyl phosphite, P(OCH<sub>3</sub>)<sub>3</sub>, is also used since unlike phosphoric acid its shift ( $\delta = 140$  ppm) is not dependent on concentration or pH. As in <sup>1</sup>H NMR, positive chemical shifts correspond to a downfield shift from the standard. However, prior to the mid-1970s, the convention was the opposite. As a result, older texts and papers report shifts using the opposite sign. Chemical shifts in <sup>31</sup>P NMR commonly depend on the concentration of the sample, the solvent used, and the presence of other compounds. This is because the external standard does not take into account the bulk properties of the sample. As a result, reported chemical shifts for the same compound could vary by 1 ppm or more, especially for phosphate groups (P=O). <sup>31</sup>P NMR spectra are often recorded with all proton signals decoupled, i.e., <sup>31</sup>P-{<sup>1</sup>H}, as is done with <sup>13</sup>C NMR. This gives rise to single, sharp signals per unique <sup>31</sup>P nucleus. Herein, we will consider both coupled and decoupled spectra.

### 3.7.4.3 Interpreting spectra

As in <sup>1</sup>H NMR, phosphorus signals occur at different frequencies depending on the electron environment of each phosphorus nucleus (Figure 3.116). In this section we will study a few examples of phosphorus compounds with varying chemical shifts and coupling to other nuclei.

<sup>22</sup>This content is available online at <<http://cnx.org/content/m46151/1.2/>>.

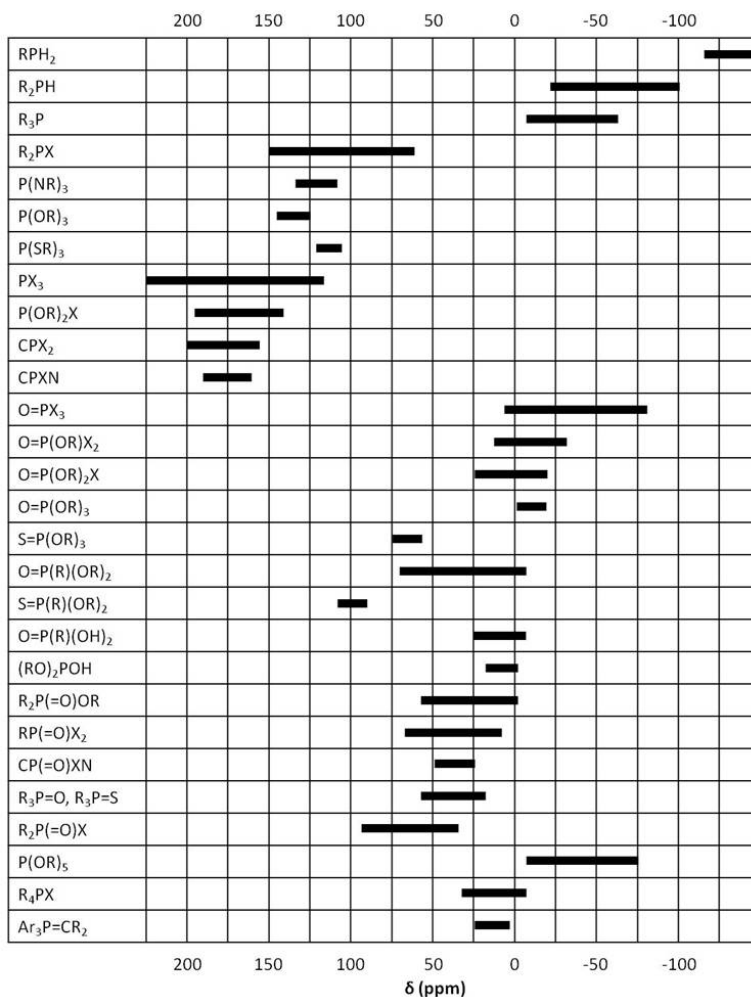
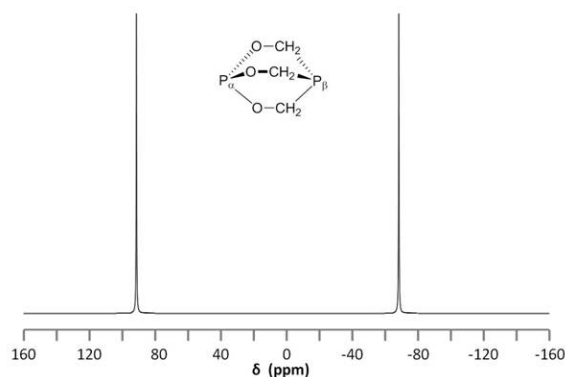


**Figure 3.116:** Chemical shift ranges for different types of phosphorus compounds.

### 3.7.4.3.1 Different phosphorus environments and their coupling to <sup>1</sup>H

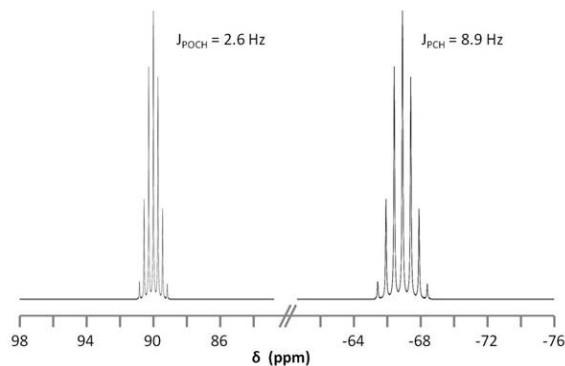
Consider the structure of 2,6,7-trioxa-1,4-diphosphabicyclo[2.2.2]octane [ $P_{\alpha}(OCH_2)_3P_{\beta}$ ] shown in Figure 3.117. The subscripts  $\alpha$  and  $\beta$  are simply used to differentiate the two phosphorus nuclei. According to Table 1, we expect the shift of  $P_{\alpha}$  to be downfield of the phosphoric acid standard, roughly around 125 ppm to 140 ppm and the shift of  $P_{\beta}$  to be upfield of the standard, between -5 ppm and -70 ppm. In the decoupled spectrum shown in Figure 3.117, we can assign the phosphorus shift at 90.0 ppm to  $P_{\alpha}$  and the shift at -67.0 ppm to  $P_{\beta}$ .





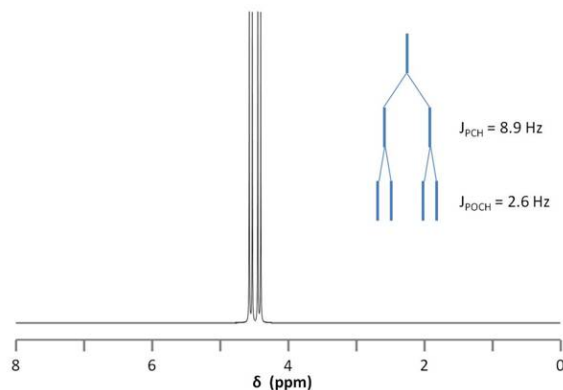
**Figure 3.117:** Structure and decoupled  $^{31}\text{P}$  spectrum ( $^{31}\text{P}\{-^1\text{H}\}$ ) of  $\text{P}_\alpha(\text{OCH}_2)_3\text{P}_\beta$ .

Figure 3.118 shows the coupling of the phosphorus signals to the protons in the compound. We expect a stronger coupling for  $\text{P}_\beta$  because there are only two bonds separating  $\text{P}_\beta$  from  $\text{H}$ , whereas three bonds separate  $\text{P}_\alpha$  from  $\text{H}$  ( $J_{\text{PCH}} > J_{\text{POCH}}$ ). Indeed,  $J_{\text{PCH}} = 8.9 \text{ Hz}$  and  $J_{\text{POCH}} = 2.6 \text{ Hz}$ , corroborating our peak assignments above.



**Figure 3.118:** The  $^{31}\text{P}$  spin coupled spectrum of  $\text{P}_\alpha(\text{OCH}_2)_3\text{P}_\beta$ .

Finally, Figure 3.119 shows the  $^1\text{H}$  spectrum of  $\text{P}_\alpha(\text{OCH}_2)_3\text{P}_\beta$  (Figure 3.120), which shows a doublet of doublets for the proton signal due to coupling to the two phosphorus nuclei.



**Figure 3.119:**  $^1\text{H}$  spectrum of  $\text{P}_\alpha(\text{OCH}_2)_3\text{P}_\beta$  and proton splitting pattern due to phosphorus.

As suggested by the data in Figure 3.116 we can predict and observe changes in phosphorus chemical shift by changing the coordination of P. Thus for the series of compounds with the structure shown in Figure 3.120 the different chemical shifts corresponding to different phosphorus compounds are shown in Table 3.20.

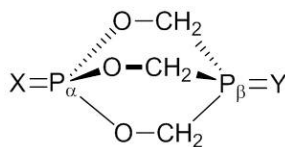


**Figure 3.120:** Structure of  $[\text{XP}_\alpha(\text{OCH}_2)_3\text{P}_\beta\text{Y}]$ .

X	Y	$\text{P}_\alpha$ chemical shift (ppm)	$\text{P}_\beta$ chemical shift (ppm)
-	-	90.0	-67.0
O	O	-18.1	6.4
S	-	51.8	-70.6

**Table 3.20:**  $^{31}\text{P}$  chemical shifts for variable coordination of  $[\text{XP}_\alpha(\text{OCH}_2)_3\text{P}_\beta\text{Y}]$  (Figure 3.120). Data from K. J. Coskran and J. G. Verkade, *Inorg. Chem.*, 1965, **4**, 1655.

### 3.7.4.3.2 Coupling to fluorine

$^{19}\text{F}$  NMR is very similar to  $^{31}\text{P}$  NMR in that  $^{19}\text{F}$  has spin  $1/2$  and is a 100% abundant isotope. As a result,  $^{19}\text{F}$  NMR is a great technique for fluorine-containing compounds and allows observance of P-F coupling. The coupled  $^{31}\text{P}$  and  $^{19}\text{F}$  NMR spectra of ethoxybis(trifluoromethyl)phosphine,  $\text{P}(\text{CF}_3)_2(\text{OCH}_2\text{CH}_3)$ , are shown in Figure 3.121. It is worth noting the splitting due to  $J_{\text{PCF}} = 86.6$  Hz.

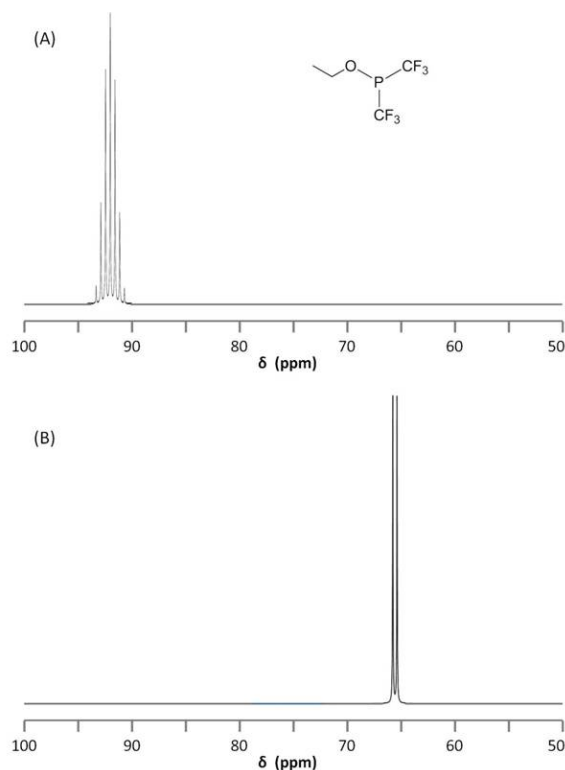


**Figure 3.121:** Structure,  $^{31}\text{P}\{-^1\text{H}\}$  spectrum (A), and  $^{19}\text{F}\{-^1\text{H}\}$  spectrum (B) for  $\text{P}(\text{CF}_3)_2(\text{OCH}_2\text{CH}_3)$ . Data from K. J. Packer, *J. Chem. Soc.*, 1963, 960.

#### 3.7.4.3.3 $^{31}\text{P}\text{-}^1\text{H}$ coupling

Consider the structure of dimethyl phosphonate,  $\text{OPH}(\text{OCH}_3)_2$ , shown in Figure 3.122. As the phosphorus nucleus is coupled to a hydrogen nucleus bound directly to it, that is, a coupling separated by a single bond, we expect  $J_{\text{PH}}$  to be very high. Indeed, the separation is so large (715 Hz) that one could easily mistake the split peak for two peaks corresponding to two different phosphorus nuclei.

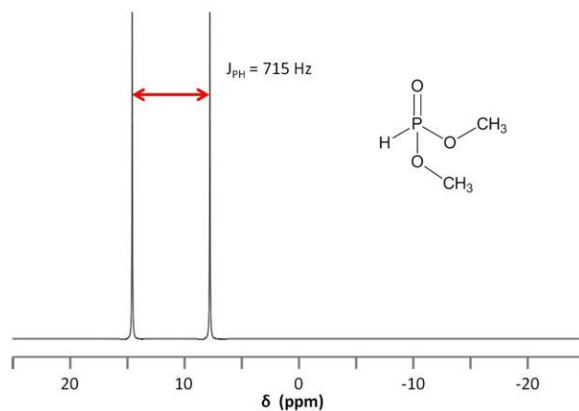


**Figure 3.122:** Structure and  $^{31}\text{P}$  NMR spectrum of  $\text{OPH}(\text{OCH}_3)_2$  with only the  $\text{OCH}_3$  protons decoupled.

This strong coupling could also lead us astray when we consider the  $^1\text{H}$  NMR spectrum of dimethyl phosphonate (Figure 3.123). Here we observe two very small peaks corresponding to the phosphine proton. The peaks are separated by such a large distance and are so small relative to the methoxy doublet (ratio of 1:1:12), that it would be easy to confuse them for an impurity. To assign the small doublet, we could decouple the phosphorus signal at 11 ppm, which will cause this peak to collapse into a singlet.

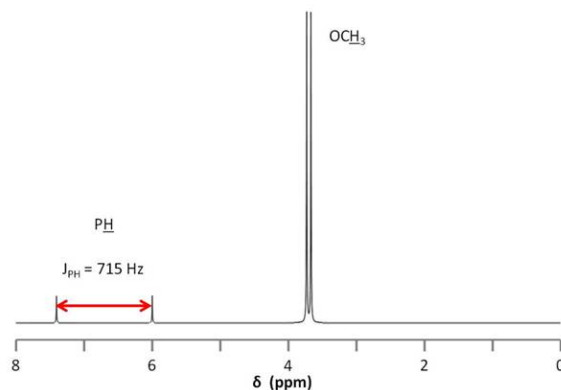


**Figure 3.123:**  $^1\text{H}$  spectrum of  $\text{OPH}(\text{OCH}_3)_2$ . Data from K. Moedritzer, *J. Inorg. Nucl. Chem.*, 1961, **22**, 19.

### 3.7.4.4 Obtaining $^{31}\text{P}$ spectra

#### 3.7.4.4.1 Sample preparation

Unlike  $^{13}\text{C}$  NMR, which requires high sample concentrations due to the low isotopic abundance of  $^{13}\text{C}$ ,  $^{31}\text{P}$  sample preparation is very similar to  $^1\text{H}$  sample preparation. As in other NMR experiments, a  $^{31}\text{P}$  NMR sample must be free of particulate matter. A reasonable concentration is 2-10 mg of sample dissolved in 0.6-1.0 mL of solvent. If needed, the solution can be filtered through a small glass fiber. Note that the solid will not be analyzed in the NMR experiment. Unlike  $^1\text{H}$  NMR, however, the sample does **not** to be dissolved in a deuterated solvent since common solvents do not have  $^{31}\text{P}$  nuclei to contribute to spectra. This is true, of course, only if a  $^1\text{H}$  NMR spectrum is not to be obtained from this sample. Being able to use non-deuterated solvents offers many advantages to  $^{31}\text{P}$  NMR, such as the simplicity of assaying purity and monitoring reactions, which will be discussed later.

#### 3.7.4.4.2 Instrument operation

Instrument operation will vary according to instrumentation and software available. However, there are a few important aspects to instrument operation relevant to  $^{31}\text{P}$  NMR. The instrument probe, which excites nuclear spins and detects chemical shifts, must be set up appropriately for a  $^{31}\text{P}$  NMR experiment. For an instrument with a multinuclear probe, it is a simple matter to access the NMR software and make the switch to a  $^{31}\text{P}$  experiment. This will select the appropriate frequency for  $^{31}\text{P}$ . For an instrument which has separate probes for different nuclei, it is imperative that one be trained by an expert user in changing the probes on the spectrometer.

Before running the NMR experiment, consider whether the  $^{31}\text{P}$  spectrum should include coupling to protons. Note that  $^{31}\text{P}$  spectra are typically reported with all protons decoupled, i.e.,  $^{31}\text{P}\{-^1\text{H}\}$ . This is usually the default setting for a  $^{31}\text{P}$  NMR experiment. To change the coupling setting, follow the instructions specific to your NMR instrument software.

As mentioned previously, chemical shifts in  $^{31}\text{P}$  NMR are reported relative to 85% phosphoric acid. This must be an external standard due to the high reactivity of phosphoric acid. One method for standardizing an experiment uses a coaxial tube inserted into the sample NMR tube (Figure 3.124). The 85%  $\text{H}_3\text{PO}_4$  signal will appear as part of the sample NMR spectrum and can thus be set to 0 ppm.